INL/EXT-13-30316
Revision 0

Light Water Reactor Sustainability Program

Grizzly Year-End Progress Report

September 2013

DOE Office of Nuclear Energy

DISCLAIMER

This information was prepared as an account of work sponsored by an agency of the U.S. Government. Neither the U.S. Government nor any agency thereof, nor any of their employees, makes any warranty, expressed or implied, or assumes any legal liability or responsibility for the accuracy, completeness, or usefulness, of any information, apparatus, product, or process disclosed, or represents that its use would not infringe privately owned rights. References herein to any specific commercial product, process, or service by trade name, trade mark, manufacturer, or otherwise, do not necessarily constitute or imply its endorsement, recommendation, or favoring by the U.S. Government or any agency thereof. The views and opinions of authors expressed herein do not necessarily state or reflect those of the U.S. Government or any agency thereof.

INL/EXT-13-30316
Revision 0

Light Water Reactor Sustainability Program

Grizzly Year-End Progress Report

Benjamin Spencer (INL), Yongfeng Zhang (INL), Pritam Chakraborty (INL), S. Bulent Biner (INL), Marie Backman (UTK), Brian Wirth (UTK), Stephen Novascone (INL), Jason Hales (INL)

September 2013

Idaho National Laboratory
Idaho Falls, Idaho 83415

http://www.inl.gov/lwrs

Prepared for the
U.S. Department of Energy
Office of Nuclear Energy
Under DOE Idaho Operations Office
Contract DE-AC07-05ID14517

EXECUTIVE SUMMARY

The Grizzly software application is being developed under the Light Water Reactor Sustainability (LWRS) program to address aging and material degradation issues that could potentially become an obstacle to life extension of nuclear power plants beyond 60 years of operation. Grizzly is based on INL's MOOSE multiphysics simulation environment, and can simultaneously solve a variety of tightly coupled physics equations, and is thus a very powerful and flexible tool with a wide range of potential applications. Grizzly, the development of which was begun during fiscal year (FY) 2012, is intended to address degradation in a variety of critical structures.

The reactor pressure vessel (RPV) was chosen for an initial application of this software. Because it fulfills the critical roles of housing the reactor core and providing a barrier to the release of coolant, the RPV is clearly one of the most safety-critical components of a nuclear power plant. In addition, because of its cost, size and location in the plant, replacement of this component would be prohibitively expensive, so failure of the RPV to meet acceptance criteria would likely result in the shutting down of a nuclear power plant.

During service, the RPV is subjected to intense neutron flux. This flux, combined with thermal aging affects, has an embrittling effect on the RPV steel, which is manifested as an increase in the brittle/ductile transition temperature of that material. This means that at a given temperature, aging effects cause the steel to have a lower toughness and tend to fracture in a more brittle manner.

The current practice used to perform engineering evaluations of the susceptibility of RPVs to fracture is to use the ASME Master Fracture Toughness Curve (ASME Code Case N-631 Section III), which provides the fracture toughness as a function of temperature. This is used in conjunction with empirically based models that describe the evolution of this curve due to embrittlement in terms of a transition temperature shift. These models are based on an extensive database of surveillance coupons that have been irradiated in operating nuclear power plants, but this data is limited to the lifetime of the current reactor fleet. This is an important limitation when considering life extension beyond 60 years. The currently available data cannot be extrapolated with confidence further out in time because there is a potential for additional damage mechanisms (i.e. late blooming phases) to become active later in life beyond the current operational experience.

To improve our understanding of the degradation of RPV steels under the conditions that would be seen under extended service life, science-based predictive modeling at the atomistic scale is needed. This modeling, combined with the limited applicable experimental data in the regime of interest, can provide understanding of the fundamental degradation mechanisms, with the goal of eventually informing models that can be useful for engineering-scale evaluations of RPVs.

To develop a tool that can eventually serve a role in decision-making, it is clear that research and development must be performed at multiple scales. At the engineering scale, a multiphysics analysis code that can capture the thermomechanical response of the RPV under accident conditions, including detailed fracture mechanics evaluations of flaws with arbitrary geometry and orientation, is needed to assess whether the fracture toughness, as defined by the master curve, including the effects of embrittlement, is exceeded. At the fracture test specimen scale, there is a need to better understand the mechanisms leading to the transition from ductile to brittle fracture. Improved modeling at this scale is important to enable the results of lower length scale modeling to inform modeling at the engineering scale. At the atomistic scale, the fundamental mechanisms of degradation need to be understood, including the effects of that degradation on the relevant material properties. Work is currently being conducted at all of these scales toward the ultimate goal of creating a usable engineering tool informed by lower length-scale modeling. This report summarizes progress made in these efforts during FY 2013.

CONTENTS

EXECUTIVE SUMMARY ii

FIGURES v

TABLES vii

ACRONYMS viii

1. Introduction 1

2. Engineering-scale Capability Development 2

    2.1 Global RPV Thermomechanical Model Benchmarking 2

    2.2 Local Submodeling 5

    2.3 Fracture Contour Integral Evaluation 8

    2.4 Engineering Scale Modeling Summary 11

3. Ductile to Brittle Transition Modeling for RPV Steels 12

    3.1 Introduction 12

    3.2 Constitutive modeling of ductile to brittle transition of fracture 13

        3.2.1 Gurson and Beremin models 13
        3.2.2 Unified Cohesive Zone Model (CZM) for Ductile to Brittle Fracture Transition: . 15

    3.3 Ductile to Brittle Transition Modeling Summary 18

4. Precipitation Kinetics and Aging Modeling for RPV Steels 19

    4.1 Introduction 19

    4.2 Method development 20

        4.2.1 Molecular dynamics (MD) 20
        4.2.2 Metropolis Monte Carlo (MMC) 20
        4.2.3 Atomic Kinetic Monte Carlo Model (AKMC) 20

    4.3 Results and Discussion 23

        4.3.1 Segregation energies from MD simulations 23
        4.3.2 Heterogeneous precipitation from MMC simulations 27
        4.3.3 Precipitation kinetics from AKMC simulations 30

    4.4 Conclusions 32

5. Summary 33

6. References 34

FIGURES

Figure 1: Temperature and pressure history applied as boundary conditions to inner surface of RPV model 3

Figure 2: Through-wall temperature profiles at various times showing comparisons between Grizzly and FAVOR solutions 3

Figure 3: Through-wall hoop stress profiles at various times showing comparisons between Grizzly and FAVOR solutions 4

Figure 4: Time history of hoop stress at inner wetted surface showing comparison between Grizzly and FAVOR solutions 4

Figure 5: Overview (left) and detailed view (right) of demonstration 3D fracture mechanics submodel embedded in global RPV model. Overview shows global model as surface without element edges, while detailed view shows wireframe global RPV mesh overlaid on local model, where surfaces used to apply boundary conditions are color-coded. 6

Figure 6: Contour plot of zz (axial) component of stress showing submodel, from interior of global model, for which exterior surface is shown with same stress contour. 7

Figure 7: Contour plot of zz (axial) component stress in submodel showing (left) overview and (right) detailed view of crack region as seen from interior surface of RPV. 7

Figure 8. Representative contour plot of the magnitude of ***q*** on a 2D domain with a crack tip located at the bottom center of the domain. 9

Figure 9. Diagram of 2D benchmark problem. 10

Figure 10. Displacement field for benchmark problem. Note that displaced mesh is magnified by 100 for illustrative purposes. 10

Figure 11: Flow stress for different temperatures [20]. 14

Figure 12: Comparison with experiments: (a) Predicted fracture toughness (b) Stable crack growth. 15

Figure 13: Schematic of unified traction separation law. 16

Figure 14: Comparison of Load-CMOD between CZM based FE simulation and experiment for T=20°C. 16

Figure 15: Unified CZM for T=-100°C: (a) Traction-separation law (b) Load-CMOD. 17

Figure 16: Unified CZM parameters for varying temperature and failure probability. Cross denotes calibration points. 17

Figure 17: Comparison with experiments: (a) Fracture toughness (b) Stable crack growth. 18

Figure 18: (a) number of mobile and absorbed vacancies as functions of KMC steps; (b) atomic configuration at 10000 KMC step. Blue atoms represent vacancies absorbed by the sink and red atoms represent currently mobile ones in the system. 22

Figure 19: Atomic stress as a function of vacancy loop radius from MD and KMC (Stroh formalism) calculation for a spherical SIA loop. The loop radius is 2.0 nm 23

Figure 20: Binding energies of a Cu solute atom with a point defect or another Cu solute atom, as functions of distance. 24

Figure 21: (a) Atomic configurations of an edge (left) and a screw (right) dislocation, with the atoms colored by segregation energies, (b) Lattice constant of bcc Fe as a function of Cu concentration, and (c) the segregation energies of Cu near an edge and a screw dislocation as functions of distances from the dislocation core. The solid and dash curves represent the linear-elastic estimation. 25

Figure 22: (a) Cu segregation energies as functions of distances from the edges of vacancy (V_loop) and SIA loops (SIA_loop) and (b) the hydrostatic pressure for SIA loops of different sizes. Symbols represent MD results and the curves are from Stroh formalism. 26

Figure 23: Cu segregation energies at different lattice defects including edge dislocation, defect loops and void. The dash line shows the edges of defect loops and the void surface. 27

Figure 24: Atomic configurations to demonstrate the Cu precipitation around an edge dislocation at (a) 0, (b) 2.5 million and (C) 5 million MMC steps. Cu atoms are show in blue and non-BCC Fe atoms in gray spheres which indicate the dislocation and the constrained layers at the top and the bottom of the simulation cell. 28

Figure 25: Atomic configurations to demonstrate the Cu precipitation around a 2.0 nm SIA loop at (a) 0, (b) 2.5 million and (c) 5 million MMC steps; and those for a 10.0 nm at (d) 0, (e) 2.5 million and (f) 5 million MMC steps. bcc-Cu atoms are show in blue; non-bcc Cu atoms are shown in yellow; and non-bcc Fe atoms (indicating SIA loops) are shown in gray spheres. 29

Figure 26: Atomic configurations to demonstrate the Cu precipitation around a 2.0 nm void at (a) 0, (b) 2.5 million and (c) 5 million MMC steps. bcc Cu atoms are show in blue; non-bcc Cu atoms are shown in yellow; and non-bcc Fe atoms (indicating the void) are shown in gray spheres 29

Figure 27: (a) Volumetric density (N_{crp}) and (b) average size ($<R_{crp}>$) of CRPs as functions of KMC time.31

Figure 28: Atomic configurations of the system with an edge dislocation at (a) 0, (b) 0.03 and (c) 0.07 seconds in KMC time. Cu clusters with 20 or more atoms are shown in red and other Cu atoms in blue. Fe atoms are omitted for clarity. The position of the dislocation core is shown in (a)............ 31

TABLES

Table 1. Comparison of J values between Grizzly calculations and the analytical solution...................... 11

ACRONYMS

AKMC	Atomic Kinetic Monte Carlo
EONY	Eason, Odette, Nanstad and Yamamoto [1] model
FAVOR	Fracture Analysis of Vessels – Oak Ridge
LWRS	Light Water Reactor Sustainability
MD	Molecular Dynamics
MMC	Metropolis Monte Carlo
PTS	Pressurized Thermal Shock
RPV	Reactor Pressure Vessel

Grizzly Year-End Progress Report

1. Introduction

The Grizzly application is being developed to simulate nuclear power plant component aging and degradation in support of the Light Water Reactor Sustainability (LWRS) program. Grizzly will ultimately provide capabilities for multidimensional, multiphysics modeling of the response of a variety of degraded systems, structures, and components in nuclear power plants to scenarios that would potentially impact their ability to perform their intended roles. These components include reactor pressure vessels (RPVs), steel and concrete containment vessels, core internal structures, other concrete structures, and cabling.

Grizzly is in its second year of development. In the first year, an initial proof of concept demonstration was performed to demonstrate Grizzly's ability to model a degraded reactor pressure vessel (RPV) under pressurized thermal shock (PTS) loading conditions. A full 3D model of the RPV vessel (without the stainless steel liner) was subjected to uniform thermal and pressure boundary conditions on the inner surface under two accident scenarios. Grizzly was used to solve the coupled thermal and mechanical response of the system. In addition, the model of Eason, Odette, Nanstad and Yamamoto [1,2], referred to here as the EONY model, was incorporated into Grizzly to predict the embrittlement of the RPV steel due to thermal aging and radiation damage. The EONY model is a "physically motivated, empirically calibrated" model that represents the degradation as a shift in the ductile to brittle transition temperature of the steel, and is based on experimental data, which only goes back to the lifespan of the longest-operating reactors. Using the EONY model to evaluate RPVs subjected to beyond 60 years of operation, which is the goal of the LWRS program, would significantly exceed the range of applicability of this model. While the transition temperature shift was calculated in the first-year demonstration of Grizzly, it was not actually used to determine whether a vessel would fail in an accident scenario. To assess whether a vessel would fail, the local response in the region of a postulated pre-existing flaw would need to be calculated to determine the stress intensity factor, which could then be compared with the fracture toughness of the embrittled material (obtained from the fracture master curve and the transition temperature shift calculated by the EONY model).

In the current year of this project, work has proceeded toward two general goals: to enhance Grizzly to permit it to be used for an engineering scale fracture assessment of an embrittled RPV, and to develop methods to characterize material evolution during irradiation and thermal aging with the goal of developing science-based methods to characterize embrittlement for time frames beyond the lifetime of the current reactor fleet. The material characterization work occurred at two levels: at the continuum scale, where models were developed to model the ductile to brittle transition in fracture tests, and at the atomistic scale, where molecular dynamics (MD), Metropolis Monte Carlo (MMC), and Atomic Kinetic Monte Carlo (AKMC) models were used to model precipitation kinetics and aging processes.

This report is organized according to these modeling scales. Section 2 documents the work toward the goal of developing needed capabilities in Grizzly to make it a usable tool for engineering fracture assessments of RPVs. Section 3 documents the fracture-test-scale continuum modeling work toward the goal of reproducing the fracture master curve of RPV steel based on fundamental material properties. Section 4 presents the atomistic scale modeling of material evolution during irradiation and thermal aging. Finally, Section 5 summarizes this report.

2. Engineering-scale Capability Development

In the current year of this project, development has been performed at the engineering scale to improve and benchmark global Grizzly RPV solutions and work toward adding needed capabilities to enable it to be used for assessments of the susceptibility of degraded RPVs to fracture during postulated PTS loading scenarios. In the previous year, which was the first year of this project, an initial proof of concept application of Grizzly demonstrated that it could be used to solved the coupled thermal and mechanical response of the RPV under such loading conditions, that the fluence could be represented on a full 3D model of the RPV, and that the resulting steel embrittlement could be calculated using the EONY model. While these are important and needed capabilities, they do not provide the complete set of code features needed to assess whether an embrittled RPV will fail due to crack growth and propagation at a flaw in the vessel.

Work has been performed in the current year at the engineering scale in three general areas: benchmarking solutions of the global RPV model, demonstrating a 3D submodeling capability for detailed solutions in the vicinity of an arbitrarily-oriented flaw, and progress toward a capability to evaluate fracture contour integrals. Some of this, notably the work on contour integrals, is still in progress, but when completed, it will be able to be combined to perform full 3D fracture assessments of arbitrarily oriented flaws at arbitrary locations in a RPV.

2.1 Global RPV Thermomechanical Model Benchmarking

To gain confidence in the models and methods used in Grizzly, benchmark cases were run against finite element solutions from the FAVOR (Fracture Analysis of Vessels – Oak Ridge) [3] probabilistic fracture mechanics code. Two-dimensional axisymmetric and three-dimensional models of the beltline region were used in Grizzly to compare to the through-thickness axisymmetric one-dimensional pressure vessel model in FAVOR.

The pressure vessel beltline model has a thickness of 20 cm and is covered at the inner surface by a 4 mm thick stainless steel clad. The stainless steel clad is a new feature of these models that was not considered in the first year of this work. The mesh of the quasi-two-dimensional model used in Grizzly for comparison with FAVOR had 19 gradually longer elements in the radial direction (the two innermost for the clad) and one element in the axial direction. A special multi-point constraint was developed in Grizzly to permit the top surface of the cylinder model to move vertically due to the effects of thermal strain and internal pressure, but constrain that surface to move as a horizontal plane, as if attached to the pressure vessel head.

The input material properties – temperature and material dependent Young's modulus, coefficient of thermal expansion, thermal conductivity and specific heat – were set to be the same in both finite element codes. Uniform pressure and temperature histories of the coolant were applied as boundary conditions at the inner surface of the RPV model, using a time-dependent heat transfer coefficient calculated by the RELAP 5 code. Figure 1 shows the pressure and temperature history used in this benchmark problem, which is considered to be a thermally driven scenario because it has a rapid temperature drop, which results in high thermal gradient and thermal stresses, but relatively low internal pressure.

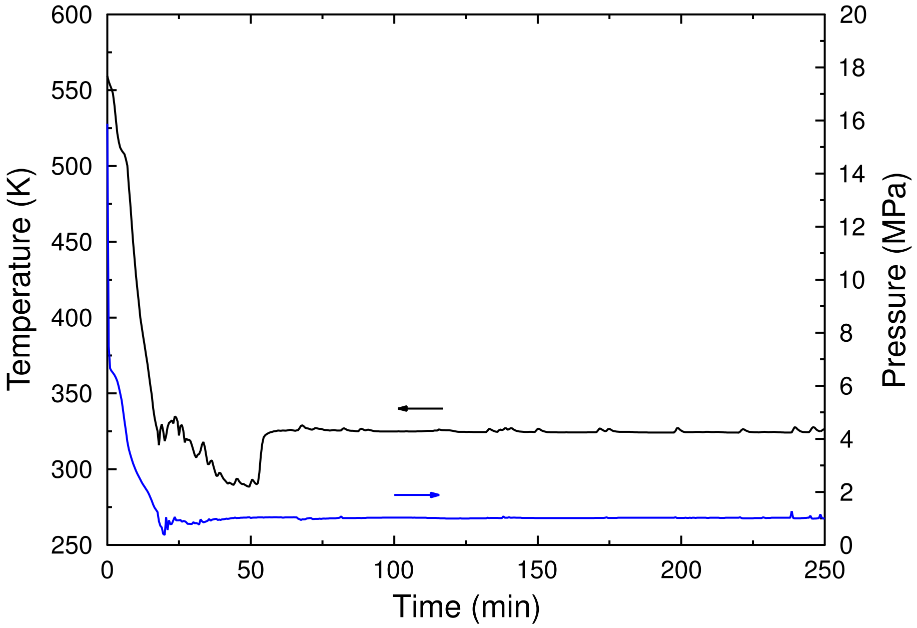

Figure 1: Temperature and pressure history applied as boundary conditions to inner surface of RPV model

Time-varying temperature and stress (axial and hoop) through the RPV wall was calculated by heat conduction and linear elastic stress analysis in the finite element meshes. FAVOR uses quadratic shape functions for the thermal and stress analysis whereas the Grizzly calculations were performed with linear shape functions. The temperature profile through the thickness of the wall is compared in Figure 2 at three different points in time. A similar comparison for the hoop stress through the wall is found in Figure 3.

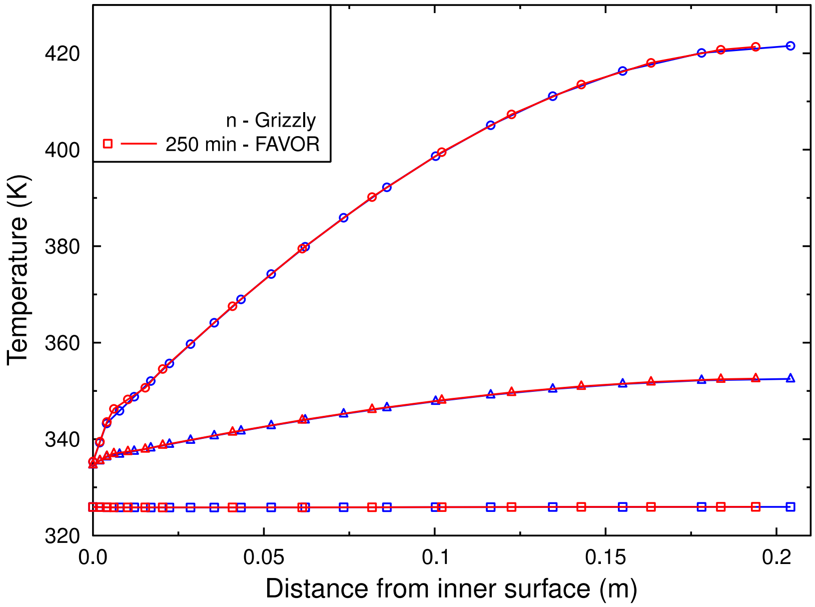

Figure 2: Through-wall temperature profiles at various times showing comparisons between Grizzly and FAVOR solutions

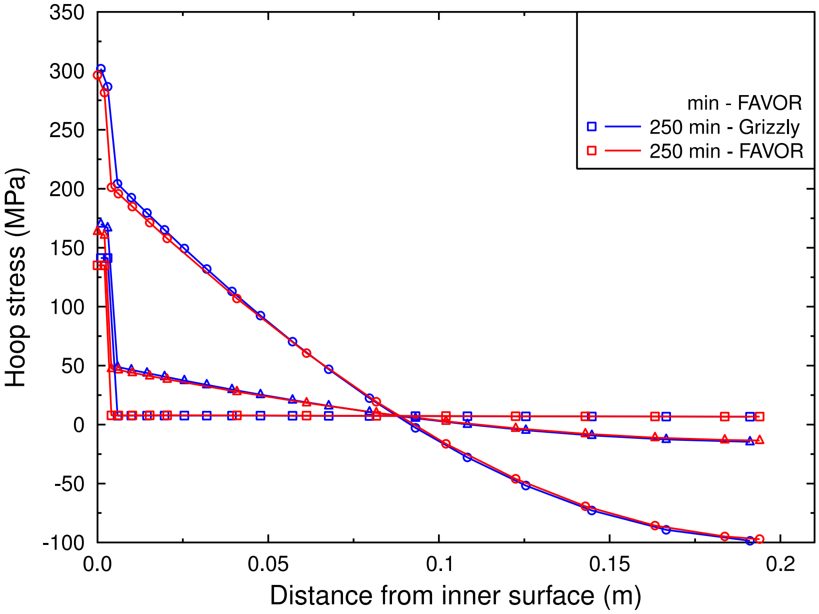

Figure 3: Through-wall hoop stress profiles at various times showing comparisons between Grizzly and FAVOR solutions

Figure 4 shows a comparison between FAVOR and Grizzly for the time history of hoop stress at the inner surface of the wall, in the stainless steel clad, where the discrepancy between the results is the largest. The inset shows the time history of the error between the solutions. The maximum discrepancy is approximately 6%.

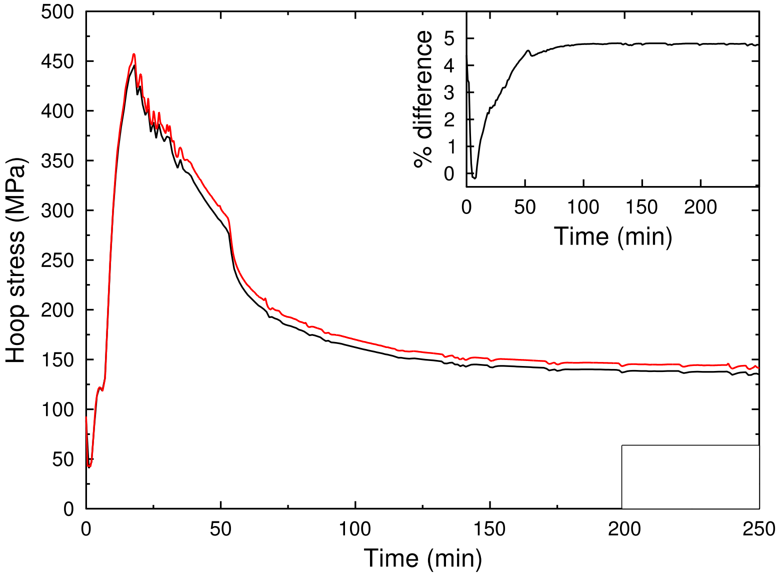

Figure 4: Time history of hoop stress at inner wetted surface showing comparison between Grizzly and FAVOR solutions

2.2 Local Submodeling

In a RPV subjected to a PTS loading scenario, the primary concern is that the loading would induce stress concentrations at the tips of pre-existing flaws that could be sufficiently high to result in the growth of one of these cracks, which could potentially propagate through the thickness of the vessel and result in a breach. To evaluate stress concentrations at crack tips requires detailed 2D or 3D models of the material in the region of the crack tip. For assessments of RPVs, this has traditionally been done by evaluating analytical fracture mechanics solutions or by developing detailed 3D fracture models, and developing influence coefficients derived from these detailed solutions that are used in conjunction with the through-wall stress profile. The FAVOR [3] code uses an extensive library influence coefficients for fracture mechanics solutions in conjunction with a 1D model of the beltline region of the RPV to evaluate the probability of failure for large numbers of postulated pre-existing flaws. This approach could be applied in Grizzly, although it is limited in that it can only be used to represent axial and radially oriented flaws. To represent general obliquely oriented flaws, it is necessary to either incorporate those flaws in the global model, or create detailed 3D submodels that contain the flaws, which are explicitly represented in the finite element submodel.

The MOOSE framework, upon which Grizzly is built, has been enhanced to be able to read any spatially- and temporally-varying solution variable from the output file from a previously run model. These solution variables can then be used for a variety of purposes in an analysis model. The ability to use this to drive boundary conditions on a 3D crack submodel embedded in a RPV has been successfully demonstrated in Grizzly. Figure 5 shows an overview of the global RPV model, showing the location of the submodel (in blue). The submodel contains a half-symmetry representation of a surface-breaking flaw, and shares the same y=0 symmetry plane used by the global model. In addition, Figure 5 shows a detailed model of the submodel, with the outside boundaries of the global model mesh shown in wireframe to illustrate the relative refinement levels of these models.

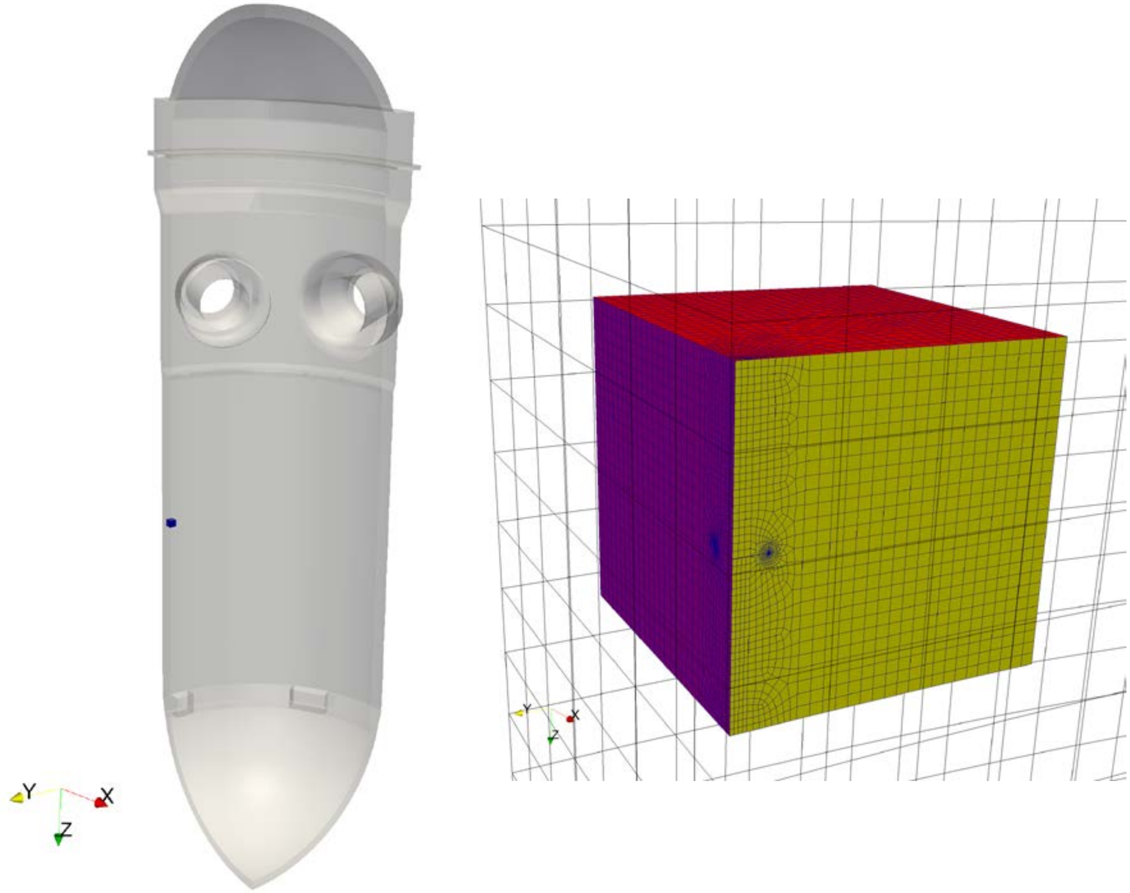

Figure 5: Overview (left) and detailed view (right) of demonstration 3D fracture mechanics submodel embedded in global RPV model. Overview shows global model as surface without element edges, while detailed view shows wireframe global RPV mesh overlaid on local model, where surfaces used to apply boundary conditions are color-coded.

In Figure 5, the surfaces of the submodel are color-coded to differentiate the surfaces to which boundary conditions are applied. The surface facing the inner wetted surface of the RPV, shown in yellow, has no prescribed displacements, but has the same pressure history that was applied to the global model applied to it. The surface on the symmetry plane, shown in magenta, has no-displacement boundary conditions in the y direction. The other four outer surfaces of the model, shown in red (only one is visible), have prescribed displacements in the x, y, and z directions using values interpolated in space and time from the solution of the global model. The crack is assumed to not affect the thermal solution of the submodel, so the temperature in the submodel is fully prescribed at every node in the model by interpolating the nodal temperatures from the global model in space and time. The submodel thus is used only to solve for the displacement degrees of freedom.

This submodeling approach was tested on a simplified submodel that did not contain a crack, and was demonstrated to behave correctly. The submodel properly captures the stress profile in the global model, but with more refinement. Once this was tested on a submodel with no crack, the cracked model was tested. The cracked model contains a blunt tip, which would be appropriate for an elastic-plastic fracture mechanics analysis. This analysis is intended only to be used as a demonstration of the submodeling capability. A more refined mesh would need to be used for an actual fracture assessment, although the same approach would be used. Figure 6 shows the zz (axial) stress contours on the outside of the submodel, as seen from the opposite side from the crack, on the interior of the RPV. This is shown together with the same stress contours on the outer surface of the global RPV model to show the equivalence of the two solutions on the boundary of the submodel, away from the crack.

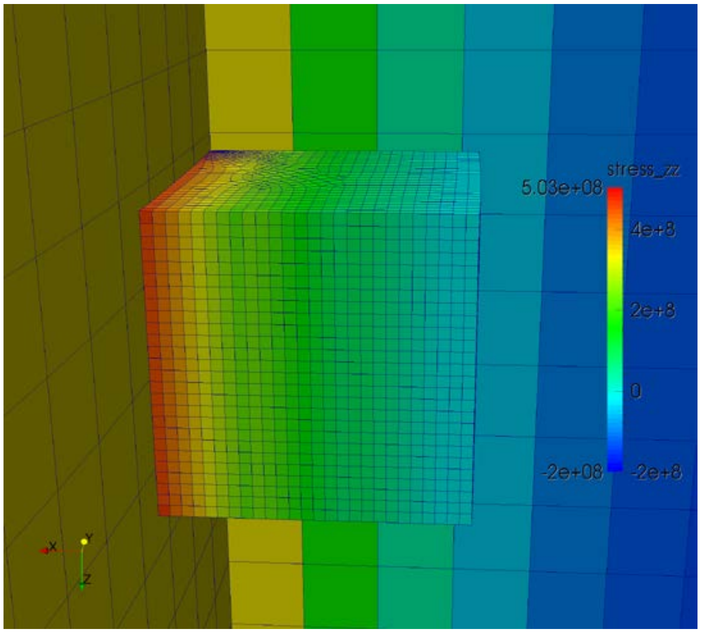

Figure 6: Contour plot of zz (axial) component of stress showing submodel, from interior of global model, for which exterior surface is shown with same stress contour.

Figure 7 shows zz (axial) stress contours for the cracked portion of the submodel, including both an overview of the entire submodel and a detailed view of the region with the crack. As expected, this clearly shows the stress concentration at the crack tip.

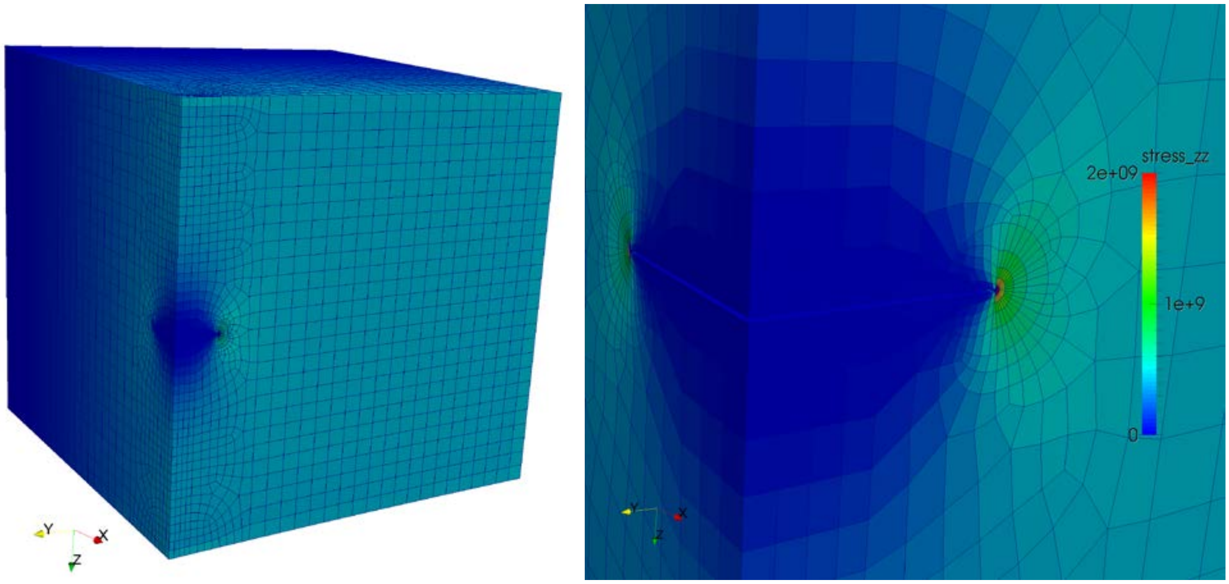

Figure 7: Contour plot of zz (axial) component stress in submodel showing (left) overview and (right) detailed view of crack region as seen from interior surface of RPV.

The ability to read displacement and temperature solutions from a global RPV model's output, and use those to drive the boundary conditions of a submodel around a flaw region has been demonstrated. As mentioned previously, at this point this is only a demonstration of the submodeling capability, and not of a detailed fracture mechanics assessment. In the next year, this will be used together with the fracture contour integral evaluation capability, which is under current development, to perform a complete fracture assessment of a degraded RPV, including embrittlement as represented with the EONY model.

To benchmark the Grizzly fracture mechanics capabilities in the next year, the WARP3D [4] code will be used for code comparisons with the fracture solutions that will be obtained from the Grizzly submodel. To this end, a capability has been developed and tested to export the boundary conditions needed to drive a fracture submodel in a format that can be used directly by WARP3D.

2.3 Fracture Contour Integral Evaluation

Linear elastic fracture mechanics (LEFM) is typically appropriate for fracture assessments of RPVs, and is performed by evaluating stress intensity at a crack location, and comparing that with measures of material toughness, which could include critical stress intensities for crack growth or arrest. The most straightforward method for evaluating the stress intensity is through the *J*-integral [5], the value of which represents the mechanical energy release rate. The *J*-integral is evaluated by performing a surface or volume integral of quantities relating to stress-work density and kinetic energy density per unit volume over a closed contour around the crack tip. The mode-*I* stress intensity factor, K_I, can be directly calculated from the mode-*I* contour integral J_I through the following relationship:

$$K_I = J_I\left(\frac{E}{1-\nu^2}\right) \tag{1}$$

The ultimate goal of this work is to develop a capability to evaluate *J*-integrals for general 3D cracks to enable fracture assessments of arbitrary crack geometries. During the current year, an initial, limited version of the *J*-integral capability has been developed and demonstrated in Grizzly for 2D small-strain problems, without considering the effects of thermal strain. This development work is in progress, and a full 3D, large deformation capability that includes thermal strain effects will developed in the next year.

Traditionally, *J* is expressed as a surface integral, but it can also be expressed as a volume integral, which lends itself to use in a finite element code. To facilitate implementation of the *J*-integral calculation into the Grizzly finite element program, the method of [6] is employed, in which J_I is represented as:

$$J_I = -\int_V (\boldsymbol{\Sigma}:\nabla\bar{q})\,dV \tag{2}$$

where $\boldsymbol{q}$ is a vector field representing contours of virtual displacements at material points due to the virtual extension of the crack front, and $\boldsymbol{\Sigma}$ is the Eshelby energy-momentum tensor [7], which can be expressed as:

$$\boldsymbol{\Sigma} = W\boldsymbol{I} - \boldsymbol{F}^T\boldsymbol{P} \tag{3}$$

where W is the stored energy density, $\boldsymbol{I}$ is the identity matrix, $\boldsymbol{F}$ is the deformation gradient, and $\mathbf{P}$ is the first Piola-Kirchoff stress.

The direction of the ***q*** vector field used in this form of the integral is constant, but the magnitude of ***q*** varies from 1 to 0 based on the distance of a point from the crack tip. Only elements in the region where the magnitude of ***q*** is between 0 and 1 contribute to a given contour integral. The user specifies the inner radius of the contour, where the magnitude of the function is 1, and the outer radius, where the magnitude is 0. This concept is applicable to both 2D and 3D models. In a 2D model, a series of concentric contours are defined for the contour integral. In a 3D model, a series of ***q*** fields would be defined to calculate the variation of *J* along the crack tip. The magnitudes of these fields would vary in a similar manner to the fields used in 2D, based on distance from the crack tip in a plane normal to the crack, but would also vary based on distance along the crack front. A representative contour plot of the magnitude of ***q*** on a 2D finite element domain with a crack tip located at the bottom center of the domain is show in Figure 8.

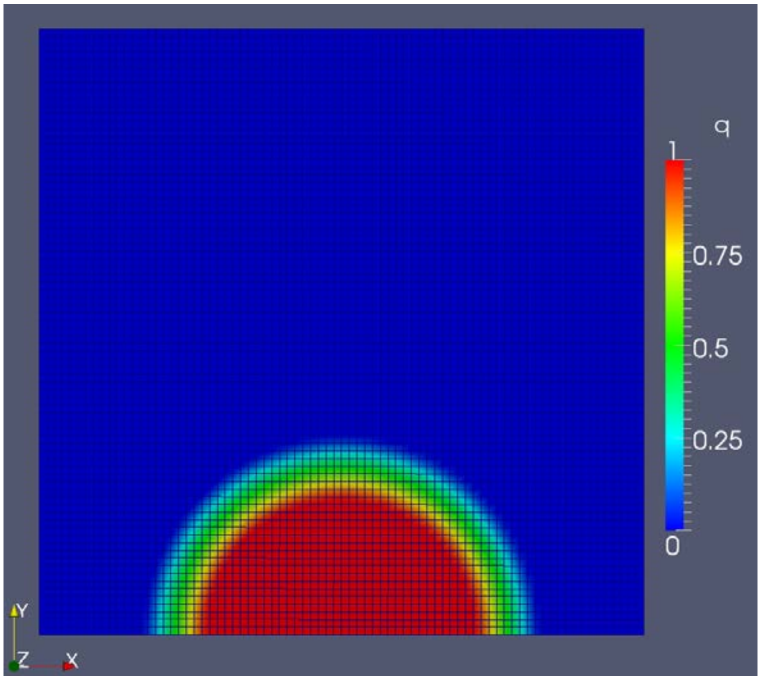

Figure 8. Representative contour plot of the magnitude of ***q*** on a 2D domain with a crack tip located at the bottom center of the domain.

The method for evaluating J_I based on equations (2) and (3) was implemented in Grizzly using a combination of modules available in that code environment. To test the *J*-integral calculation in Grizzly, a finite element model of a 2D benchmark problem with a known analytical solution [8] was created and run. The simulation is of a square domain with a center crack. Symmetry boundary conditions were applied at x = 0 and at y = 0 where x > a. A load of 100 N/mm^2 was applied to the top of the domain. Young's modulus = 207GPa and Poisson's ratio of 0.3 were used to define the mechanical properties of the domain. Linear elastic, small displacement, plane strain assumptions were applied and thermal effects ignored. A diagram of this problem is shown in Figure 9.

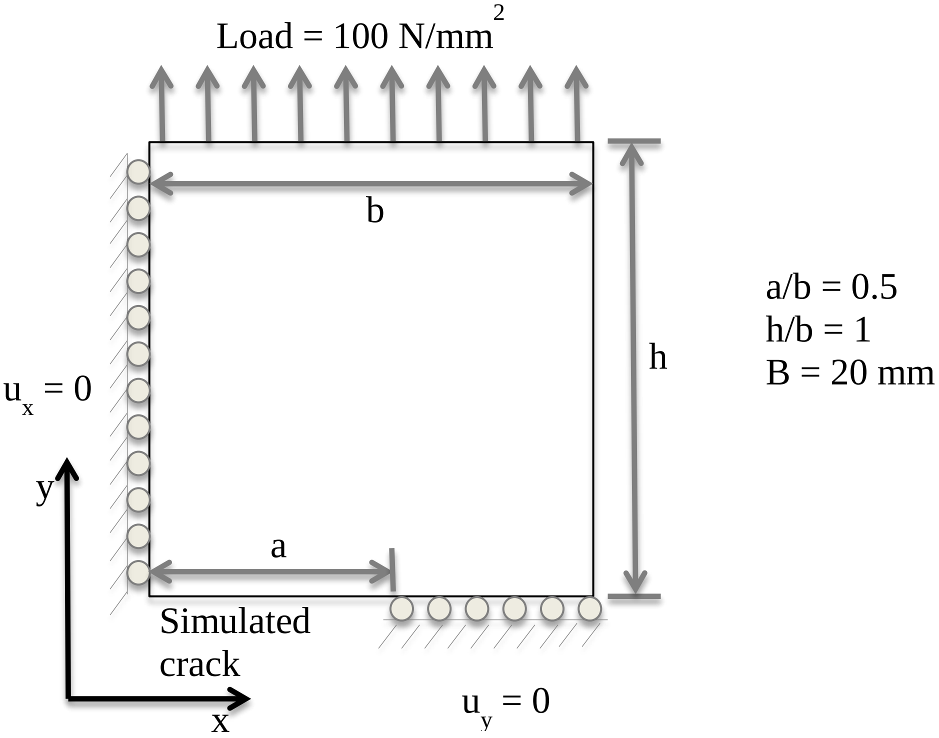
Load = 100 N/mm^2
b
h
a/b = 0.5
h/b = 1
B = 20 mm
$u_x = 0$
y
a
Simulated crack
x
$u_y = 0$

Figure 9. Diagram of 2D benchmark problem.

A contour plot of the displacement field for this problem is shown in Figure 3. Note that the displaced mesh shown in Figure 3 is scaled by a factor of 100 for illustrative purposes.

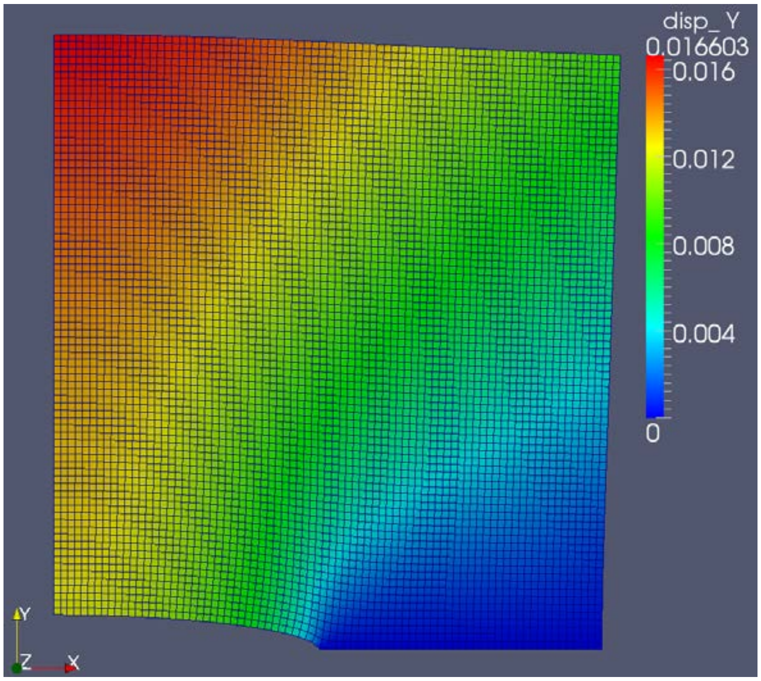

Figure 10. Displacement field for benchmark problem. Note that displaced mesh is magnified by 100 for illustrative purposes.

The analytical (or closed form) solution [8] for this linear elastic fracture mechanics problem is

$$\frac{\boldsymbol{K_I}}{\boldsymbol{K_0}} = 1.325 \tag{3}$$

where

$$\mathbf{K_0} = \boldsymbol{\sigma\sqrt{\pi a}}. \tag{4}$$

and

$$\boldsymbol{K_I} = \sqrt{\frac{\boldsymbol{J\,E}}{\boldsymbol{1 - v^2}}} \tag{5}$$

Solving for *J* with the parameters defined here gives a value of 2.425 for the analytical solution. When calculating *J* numerically, as was done in Grizzly, several *q* functions are defined with different values of inner and outer radii. In this benchmark calculation, we used five *q* functions, with different inner and outer radii (r_i, r_o) values. The values from the Grizzly and analytical calculations of *J* are shown in Table 1. The largest error in the calculated J relative to the analytical solution is 2.9%.

Table 1. Comparison of J values between Grizzly calculations and the analytical solution

(r_i, r_o) values	4, 4.5	4.5, 5	5, 5.5	5.5, 6	6, 6.5
Numerical J	2.455	2.495	2.477	2.428	2.399
Analytical J	2.425				

2.4 Engineering Scale Modeling Summary

During the current fiscal year, three main developments have been performed to provide important needed capabilities to enable Grizzly to be used for engineering fracture assessments of embrittled reactor pressure vessels. First, the results of a global thermo-mechanical model of a reactor pressure vessel subjected to pressurized thermal shock loading conditions have been benchmarked against solutions from FAVOR, a code with a significant pedigree designed specifically to solve that problem. Second, a capability to drive the boundary conditions for detailed submodels of the region surrounding a fracture has been developed and demonstrated on an example fracture problem in Grizzly. Finally, progress has been made toward developing a general fracture *J*-integral integration capability, and an initial limited capability has been demonstrated. This capability, when completed, will permit Grizzly to be used to evaluate the stress intensity on a pre-existing flaw during postulated accident conditions. During the next fiscal year, these capabilities will be combined together to demonstrate a 3D fracture assessment of an aged reactor pressure vessel subjected to pressurized thermal shock loading conditions.

3. Ductile to Brittle Transition Modeling for RPV Steels

3.1 Introduction

There has been significant effort to model the different failure mechanisms that are active at different temperature regime in RPV steels. At lower temperatures, unstable failure by cleavage fracture is identified as the dominant failure mechanism. This is characterized by slip induced micro-crack formation at carbides and their extension into macroscopic cracks depending on the local deformation state and microstructure. Physics based models have been proposed in [9-11] to explain these mechanisms of cleavage initiation in steel. However these models don't relate cleavage initiation at a microscopic length scale to the fracture toughness. To develop such a correlation, a model has been proposed in [12], in which it is assumed that cleavage failure happens when crack tip stress (σ_f) exceeds a critical value over 1 or 2 grain diameters. However this model fails to capture the scatter in fracture toughness associated with cleavage failure. Modifications have been made to this model in [13] in which a critical volume ahead of the crack tip has been considered to explain the scatter in fracture toughness due to cleavage failure. A more rigorous statistical model has been proposed by Beremin [14] in which a Weibull distribution [15] is used to relate fracture stress to failure probability at lower and transition temperatures where cleavage fracture is the dominant mechanism. The Weibull parameters are obtained from fracture tests performed at lower temperatures and are assumed to be temperature independent. The temperature dependent variation of fracture toughness is considered by modifying the flow stress of the material. Analytical solutions and FE simulations with hardening plasticity are used to obtain crack-tip stress fields. Though this model has been fairly successful in capturing the scatter in fracture toughness at and near the lower shelf, it requires the modeling of stable crack growth near the transition regime to provide accurate results. Stable crack growth primarily takes place through void nucleation, growth and coalescence. By incorporating ductile damage models proposed by Rousselier [16] or Gurson [17] to simulate stable crack growth prior to unstable failure, improved predictions can be made. In [18,19] DBT using Charpy specimens have been performed using the Rousselier model [16] in conjunction with the Beremin model [14] to predict onset of cleavage failure. Modifications have been made to the Beremin model by introducing the effect of plastic strain and history of maximum principal stress to evaluate the critical Weibull stress. Irradiation effects have also been considered in their work. DBT of German low alloy pressure vessel (PV) steel using CT-specimens have been analyzed in [20] by considering a non-local Rousselier model [21] in conjunction with the Beremin model. The non-local model eliminates the mesh-dependency typically observed in local strain-softening models. In addition to the Beremin model, a local stress based model in conjunction with Weibull distribution has also been proposed in [22] as a cleavage initiation indicator. Though these approaches have been able to capture the fracture toughness variability at and near lower shelf, an improved model consisting of both ductile and cleavage mode of crack growth is necessary to predict the entire DBT region accurately. In addition, the model should have the provision to incorporate more physical lower length scale models as in [23] and should be usable at engineering scales.

In the present work, a cohesive zone based model has been proposed to analyze DBT in RPV steel. A unified model has been developed which incorporates both ductile damage and cleavage failure mechanisms through temperature and failure probability dependent parameters. The flow stress of the bulk material is varied to obtain the temperature dependent bulk material behavior. It is assumed that without cleavage, the cohesive law follows a traction-separation behavior of ductile-damage as described in [24]. From the known flow-stress evolution at different temperatures separate ductile-damage traction-separation parameters can thus be obtained from a unit cell analysis. However depending on the temperature and failure probability, unloading in the cohesive law due to cleavage can start earlier, and can reduce the fracture toughness of the material. With the use of such a cohesive law, scatter in the fracture toughness with temperature can be successfully obtained. The results from this methodology are compared with experiments and Master Curve reported in [20].

In this report both the approaches to model DBT has been investigated. The material parameters reported in [20] for German low alloy steel has been used. A rate dependent Gurson model for ductile damage and Beremin model to predict cleavage crack initiation has been used for the first approach. For the second approach, a correlation has been derived for the unified traction separation law parameters at different temperatures and failure probabilities. Fracture toughness predictions are compared with Master curve reported in [20]. Presently ABAQUS FEM code is used to perform the simulations since the model is still under development.

3.2 Constitutive modeling of ductile to brittle transition of fracture

3.2.1 Gurson and Beremin models

This approach has been reported extensively in the literature in which ductile crack growth is explicitly captured using Gurson [17] or Rousselier model [16] and cleavage failure is predicted using the Beremin model [14] as a post-processing after the simulations.

In Gurson model for ductile damage, and the resulting crack growth happens through nucleation of voids, their subsequent growth and coalescence. Enhancements proposed in [25] considering accelerated void coalescence once a critical void volume fraction is reached has been considered also in our present work. Following large deformation theory, the plastic component of rate of deformation tensor in the rate dependent Gurson model is obtained from:

$$\boldsymbol{D}^p = \dot{\lambda}\frac{\partial \phi}{\partial \boldsymbol{\sigma}} \tag{6}$$

where the flow potential ϕ is represented by

$$\phi = \frac{\sigma_e^2}{\sigma_m^2} + 2f^* q_1 \cosh\left(\frac{q_2\sigma_h}{2\sigma_m}\right) - 1 - q_3 f^{*2} \tag{7}$$

In Equations 6-7, σ_e is the Von Mises stress, σ_h is the hydrostatic stress, σ_m is the stress in the matrix, f* is the modified void volume fraction and q_1, q_2, q_3 are parameters. The flow rate $\dot{\boldsymbol{\lambda}}$ is obtained from equivalence of plastic power. The evolution of void is governed by

$$\dot{f} = \dot{f}_g + \dot{f}_n \tag{8}$$

where void growth rate $\dot{\boldsymbol{f}}_{\boldsymbol{g}}$ is defined by

$$\dot{f}_g = (1-f)tr(\boldsymbol{D}^p) \tag{9}$$

and a strain controlled void nucleation rate $\dot{\boldsymbol{f}}_{\boldsymbol{n}}$ is defined by

$$\dot{f}_n = \frac{f_n}{s_N\sqrt{2\pi}} \exp\left(-\frac{1}{2}\left(\frac{\varepsilon_m-\varepsilon_N}{s_N}\right)^2\right)\dot{\varepsilon}_m \tag{10}$$

where f_N, s_N and ε_N are the statistical parameters describing the variations in the void nucleation sites. Accelerated coalescence of void after a critical void volume fraction is modeled using:

$$f^* = \begin{cases} f, \text{for } f \leq f_c \\ f_c + \frac{f_u - f_c}{f_f - f_c}, \text{for } f > f_c \end{cases} \tag{11}$$

where $f_u = 1/q_1$ and f_c and f_f are critical and final void volume fractions respectively.

In the Beremin model, it is assumed that unstable cleavage crack initiation happens at the weakest link. Based on the strength of the weakest link, a cumulative probability density P_f for failure is defined as:

$$P_f = 1 - \exp\left(-\int_v g(\sigma_I)\frac{dV}{V_0}\right) \tag{12}$$

where σ_I is the maximum principal stress, g is some functional form defining the strength of an infinitesimal volume and V_o is the reference volume. Weibull distribution [15] has been assumed to describe the distribution of strength in the microstructure in [14]. Using the Weibull distribution, the probability of failure P_f can be described by:

$$P_f = 1 - \exp\left(-\left(\frac{\sigma_w}{\sigma_M}\right)^m\right) \qquad where \qquad \sigma_w = \left(\int_v \sigma_I^m \frac{dV}{V_0}\right)^{\frac{1}{m}} \tag{13}$$

In our present study, the experimental results for one inch thick compact tension, 1T-CT, fracture toughness testing specimen of German low alloy steel reported in [20] have been used for comparison of simulation results with the experiments. The Weibull parameters are calibrated from fracture toughness data at temperature T=-100°C and are used in the present work. Also, an assumption similar to [20] is made i.e. Weibull parameters predicting cleavage failure are temperature independent. The calibrated Rousselier model parameters in [20] were taken for the Gurson model in the present work. The parameters q_1, q_2 and q_3 and void nucleation parameters has been considered similar to [25]. Plane strain FEM simulations for 3 different temperatures (T=-100°C, T=-60°C and T=-20°C) were performed using the rate dependent Gurson model. For the different temperatures the material flow stress varies and is shown in Figure 11. Cleavage failure initiation at P_f=5% and 95% is predicted using the Beremin model and calibrated Weibull parameters. A comparison of predicted fracture toughness and stable crack growth with experiments is shown in Figure 12 (a) and (b) respectively.

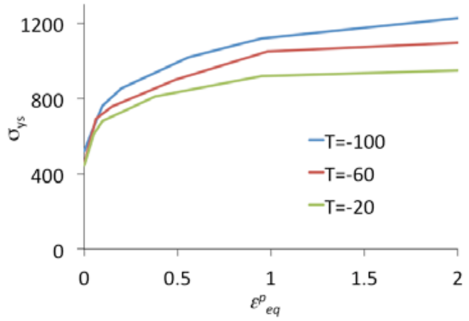

Figure 11: Flow stress for different temperatures [20].

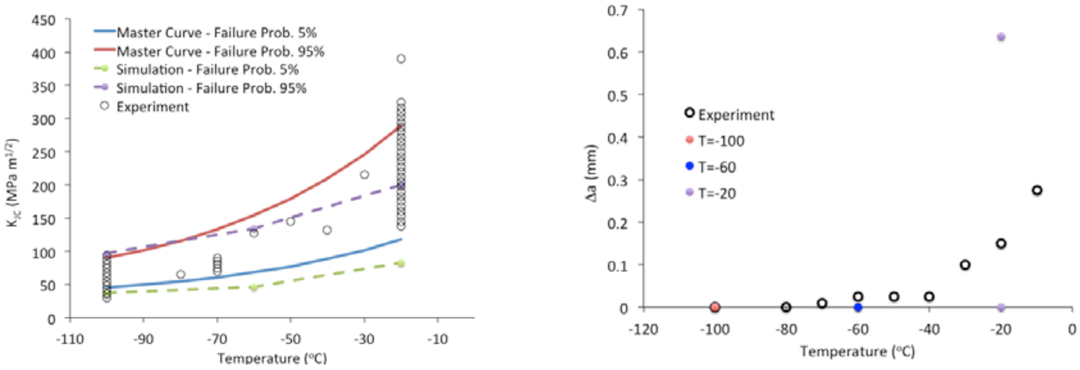

(a) (b)

Figure 12: Comparison with experiments: (a) Predicted fracture toughness (b) Stable crack growth.

As can be observed from the comparisons with the experiments, this approach is able to capture DBT with reasonable accuracy. The large difference with Master curve at higher temperature (T=-20°C) is due to the Gurson model which localizes damage evolution to a small region ahead of the crack tip (mesh dependency). Owing to such localized damage, higher stresses-state evolves near the crack tip and satisfying the cleavage failure criterion earlier. These deficiencies in the model can be somehow mitigated using a mesh size independent non-local formulation.

3.2.2 Unified Cohesive Zone Model (CZM) for Ductile to Brittle Fracture Transition:

For a material undergoing ductile damage, the underlying traction separation law consists of an initial steady state void growth and coalescence, followed by rapid coalescence and complete loss of strength once a critical void volume fraction is reached. The traction-separation law proposed in [24] has been used in the present work to represent ductile damage where the traction σ is related to the separation δ by

$$\sigma = \sigma_0 \begin{cases} 2\left(\frac{\delta}{\delta_e}\right) - \left(\frac{\delta}{\delta_e}\right)^2, \text{ where } 0 < \delta < \delta_e \\ 1, \text{ where } \delta_e < \delta < \delta_c \\ 2\left(\frac{\delta - \delta_c}{\delta_f - \delta_c}\right)^3 - 3\left(\frac{\delta - \delta_c}{\delta_f - \delta_c}\right)^2 + 1, \text{ where } \delta_c < \delta < \delta_f \end{cases} \tag{14}$$

where σ_0 is the maximum stress and δ_e, δ_c, δ_f are the separation distances when maximum stress is reached, at onset of damage (unloading) and final failure respectively. For the unified cohesive law developed in this work, it is assumed that:

(i) For a given flow stress, at a given temperature, the shape of the traction separation law is fixed by the ductile damage;
(ii) Depending on temperature and the failure probability the maximum stress at unloading (σ_{max}) and failure separation distance (δ_f) varies.
(iii) The separation distance at onset of unloading (δ_c) determines the amount of ductile damage before the cleavage failure.

A schematic of the proposed unified traction separation law is shown in Figure 13.

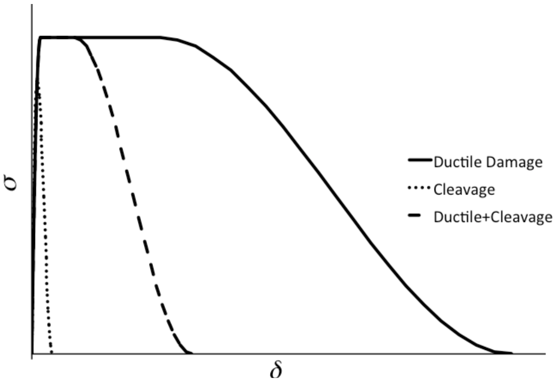

Figure 13: Schematic of unified traction separation law.

The traction separation law for cleavage failure follows a similar law as shown in Equation 14 but without the hold at σ_0 .

The cohesive zone parameters for ductile-damage are obtained from plane strain unit cell analysis with rate dependent Gurson model as the material behavior. For the unit cell analysis, a crack tip triaxiality of 3 is assumed and the stress ratio $\beta=\sigma_{11}/\sigma_{22}$ is evaluated from

$$\beta = \frac{\sqrt{3}H-1}{\sqrt{3}H+1} \tag{15}$$

where H is the triaxiality. A strain rate of 0.001 /s has been used to simulate quasi-static behavior. The Gurson model parameters described in the previous section has been used. From the unit-cell analysis the σ-ε response along the primary loading direction (22) for T=20°C (room temperature) and the corresponding fit is obtained. To use the non-dimensional traction separation law parameters in FEM simulations, a cell height h needs to be prescribed. Following [26] h=0.1 mm has been considered which is based on the microstructure. Plane strain FEM simulation is performed for the CT specimen. Comparison of Load-CMOD with experiment is shown in Figure 14. It is to be noted that the cell height used in unit cell simulations is independent of the mesh dimensions.

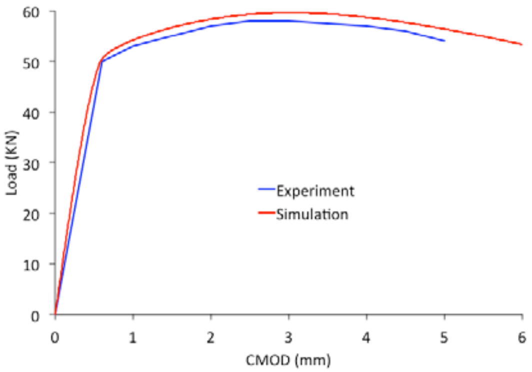

Figure 14: Comparison of Load-CMOD between CZM based FE simulation and experiment for T=20°C.

Similar ductile damage traction separation laws are obtained for T=-100°C, -60°C and -20°C. To obtain CZM parameters for cleavage failure at different probabilities and temperature, the experimental fracture toughness data at T=-100°C is used for calibration. It is assumed that the unloading slope remains constant. Hence the unified CZM only depends on a single parameter σ_{max}, which varies with temperature and failure probability. The traction separation law and Load-CMOD curves for P_f=5% and 95% at T=-100°C are shown in Figure 15 (a) and (b), respectively. Corresponding fracture toughnesses at T=-100°C can be seen in Figure 17 (a).

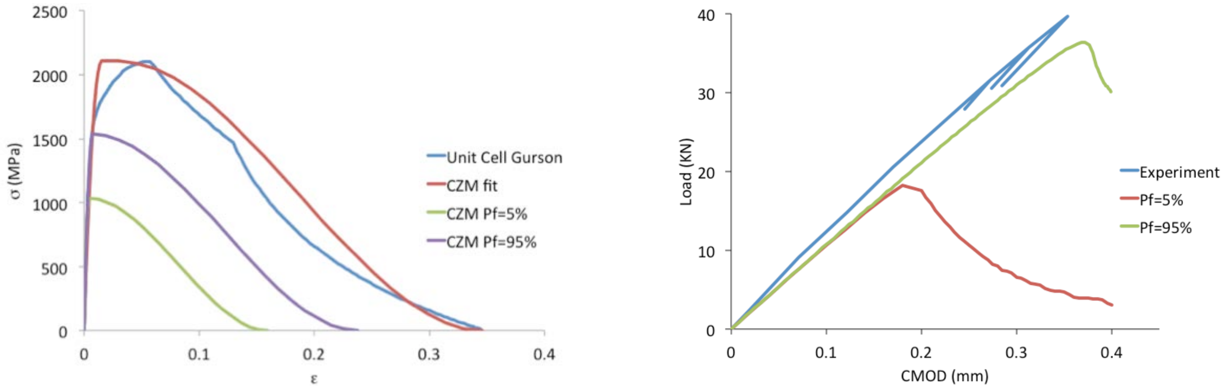

(a) (b)

Figure 15: Unified CZM for T=-100°C: (a) Traction-separation law (b) Load-CMOD.

To obtain the unified CZM parameters, the experimental fracture toughness data at T=-20°C and P_f=95% is considered additionally for calibration. A linear fit between the maximum stress of ductile damage traction-separation law (σ_0) (Equation 14) and energy release rate (G) between T=-100°C, P_f=95% and T=-20°C, P_f=95% is performed to obtain CZM parameters for varying temperature and failure probabilities and is shown in Fig. 15 . For varying failure probabilities, the slope is kept constant and intercept is evaluated from energy release rate (G) at T=-100°C. The cross in Figure 16 designates the points used for calibration.

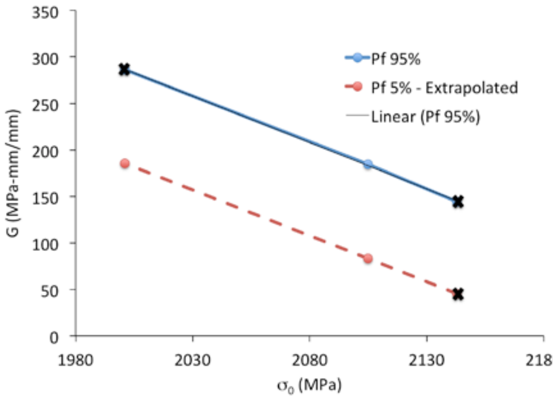

Figure 16: Unified CZM parameters for varying temperature and failure probability. Cross denotes calibration points.

A comparison of predicted fracture toughness and stable crack growth with experiments is shown in Figure 17 (a) and (b) respectively and a close agreement can be seen.

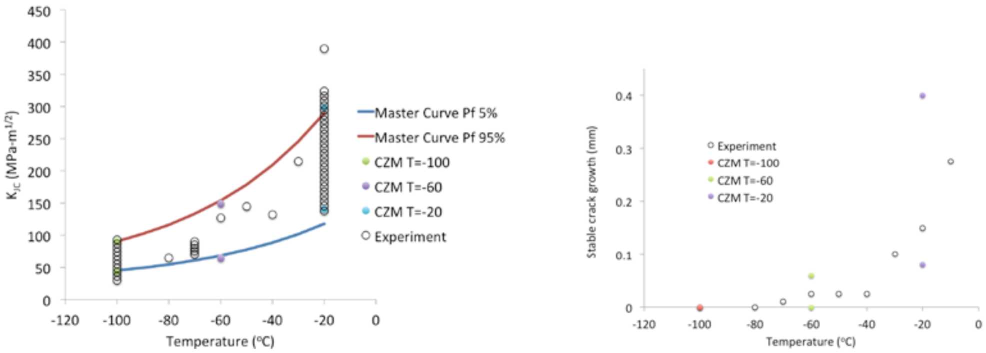

(a) (b)

Figure 17: Comparison with experiments: (a) Fracture toughness (b) Stable crack growth.

3.3 Ductile to Brittle Transition Modeling Summary

Different approaches to predict ductile to brittle transition behavior in reactor pressure vessel steels have been investigated. The first approach captures stable crack growth due to ductile damage using the Gurson model. The onset of unstable cleavage failure is predicted using the Beremin model. Reasonable agreement with experiments for 1T-CT specimen can be seen. This approach is, however, limited in its ability to accommodate lower length scale phenomena and in its usability at the engineering scale.

To overcome these limitations, a unified cohesive zone model has been developed to predict the ductile to brittle transition. A correlation has been derived to obtain parameters for this model for all temperatures and failure probabilities. This model has been demonstrated to show good agreement with experimental results for fracture toughness and stable crack growth. The ability to capture brittle to ductile transition behavior using a model that is based on fundamental material properties is important to inform engineering scale models with inputs from lower length scale modeling.

4. Precipitation Kinetics and Aging Modeling for RPV Steels

4.1 Introduction

Reactor pressure vessels in light water reactors are usually made of low-alloy steels of body-center-cubic (bcc) ferritic phase, with Mn, Ni, C and Si being the primary alloying elements, and Cu being either an alloying element or an impurity. During their prolonged service, usually on the order of tens of years, the RPVs are subject to both high temperature (about 300˚C) and radiation damage induced by fast neutrons. Long time thermal aging leads to the formation of precipitates of alloying elements, particularly Cu which is almost insoluble in bcc-Fe. On the other hand, neutron radiation produces the lattice defects such as vacancies and self-interstitial-atoms (SIAs), and their agglomerates including voids and defect loops. Both the precipitates and lattice defects will impede the dislocation motion, resulting in hardening and consequent embrittlement of RPV steels.

Depending on the chemical composition, two types of precipitates have been characterized in RPV steels, namely the Cu-rich precipitates (CRPs) in steels containing high-Cu concentrations and the Mn/Ni-rich precipitates (MNPs), i.e., the so-called late-blooming-phases, in low to no Cu containing steels [32]. The formation of CRPs has been considered as the primary cause for RPV embrittlement. The effect of MNPs, which form at high neutron fluence with longer incubation time, is currently less understood. Both types of precipitates share the same lattice structure with the bcc matrix when their sizes are small. As their sizes grow beyond a certain critical size, the CRPs experience a bcc to face-centered-cubic (fcc) phase transition [33]. However, regardless of their crystalline structures, all precipitates are obstacles to dislocation motion and thus cause hardening and embrittlement. During in service, the precipitation of alloying elements and the formation of lattice defects take place at the same time. The radiation-induced lattice defects can cause hardening and embrittlement just by themselves being also obstacles to dislocation motion. Furthermore, the irradiation-induced point defects enhance the diffusion of alloying elements, thus accelerate the precipitation kinetics. Extended defects formed by clustering of point defects, including voids and defect loops as observed in experiments, may act as preferential nucleation sites for the precipitates, in particular MNPs that are usually seen at high neutron fluence. In a combined experimental and modeling study, SIA loops have been shown to play an important role in the formation of CRPs [34]. On the other hand, the presence of alloying elements may also change the formation and growth kinetics of extended lattice defects. For instance, transmission-electron-microscopy (TEM) analysis has shown that the presence of alloying elements may delay the growth of SIA loops, resulting in smaller average size and narrower size distribution [35].

The hardening and consequent embrittlement RPV steels originate from the changes in the microstructure, i.e., precipitation and radiation damage. Both processes take place via atomic events such as diffusion and displacement of atoms. An accurate quantitative modeling requires the fundamental understanding of unit processes taken place at the atomic scale such as nucleation events and their early stable growth kinetics; and their collective and colloborative behavior with the dislocation, vacancy and self interstial atom, SIA loops. The microstructural features responsible for the property degradation are usually ranges in sizes of a few to tens of nanometers. For a predictive description, the nature and the associated spatial dimensions call for fundamental studies at the atomic scale, e.g., via the ab-initio density-functional-theory (DFT) calculations, molecular dynamics (MD) and Metropolis Monte Carlo (MMC) with empirical interatomic potentials, Lattice Monte Carlo (LKMC) or Atomic Kinetic Monte Carlo (AKMC) simulations.

In this section, we summarize our progress at the atomistic scale during FY2013.

4.2 Method development

The principal work at the atomic scale is to develop a predictive quantitative model for the microstructure evolution of RPV steels under thermal aging and neutron radiation. We have developed an AKMC method for the precipitation kinetics in bcc-Fe, with Cu, Ni, Mn and Si being the alloying elements. In addition, we used MD simulations to provide input parameters (if not available in literature). MMC simulations were also carried out to explore the possible segregation/precipitation morphologies at the lattice defects. First we briefly describe each of the simulation algorithms, then will present our results.

4.2.1 Molecular dynamics (MD)

MD simulations determine the trajectories of atoms by numerically solving the Newton's equation of motion for a system consisting of interacting atoms. The force acting on each atom is given by the inter-atomic potential, i.e., the force field, which governs the interaction of each atom with its surrounding neighbors. In our studies, MD simulations were performed using the simulation package LAMMPS developed at Sandia National Laboratories [36]. For the interatomic potential we used the embedded-atom-method (EAM) type potential developed by Bonny et al. for the Fe-Cu-Ni system [37]. This potential was derived from the Mendelev potential [38] for bcc-Fe, the Voter potential for fcc-Ni [39], and the Mishin potential [40] for fcc-Cu. The cross terms for Fe-Cu, Fe-Ni and Ni-Cu were given in Pasianot et al. [41], Bonny et al. [42], and Bonny et al. [37] respectively. The Bonny potential was "*developed in such a way that both the alloy's (Fe-Ni and Fe-Cu) thermodynamic properties and the interaction between solute atoms and point-defects are properly reproduced, compared to, respectively, the experimental phase diagram and DFT calculations*" [37]. To study of the hardening and embrittlement of RPV steels is one of the primary motivations to develop this potential. Therefore, it was chosen as the inter-atomic potential in our present work.

4.2.2 Metropolis Monte Carlo (MMC)

MMC simulations are used to explore the possible precipitation morphologies, owing to the slow kinetics, which may not be accessible with MD and AKMC simulations. To take the advantage of the large empirical potential database in LAMMPS, the MMC method used in this project is implemented as user defined subroutines to LAMMPS with three different MMC moves namely [43]:

1. Random translation of atoms, based of the probability p = exp(-ΔE/KT); here ΔE is the change in total potential energy induced by the move. K is Boltzmann constant and T temperature.

2. Swapping the positions of randomly selected two different atom types based on the probability p = exp(-ΔE/KT). This move is used to enhance the mass transport without changing the global composition.

3. Changes the type of a randomly selected atom to a desired type, to mimic a chemical interaction which changes the global composition.

Our algorithm is designed in such a way that the MC moves can be used in NVT or NPT ensembles.

4.2.3 Atomic Kinetic Monte Carlo Model (AKMC)

The development of AKMC model for the Fe-based alloy systems was the primary task at the atomic scale simulations for FY2013; therefore, it is given some more details in here. Our code development is based on the SPARKKs simulation package that uses the MPI framework developed at Sandia National Laboratories [44]. In the AKMC model [45], the microstructure of the system evolves by the jump of mobile atoms (or vacancies) within a predefined rigid-lattice framework. Off-lattice motions are currently not allowed in this algorithm. The kinetics, i.e. time evolution, can be achieved using the list of events, e.g., jump of atoms, with the probability Γ_i of each event given by:

$$\Gamma_i = \upsilon_i \exp(-\Delta E_i^m / K_B T) \tag{16}$$

Here v_i is the attempt frequency of the i-th event; ΔE_i^m is the activation barrier; T is the temperature and k_B is the Boltzmann constant. In each AKMC step, one event is chosen from the list by a weighted random selection to evolve the microstructure, therefore it is much more efficient than the MCC method, and the corresponding time increment is given by:

$$\Delta t = (\sum_i \Gamma_i)^{-1} \tag{17}$$

Ideally, all the possible events should be included into the event list, in order to achieve the correct kinetics. Furthermore, accurate attempt frequencies and activation barriers are required to obtain the correct time. The attempt rates and activation barriers can be calculated using atomistic simulations such as MD simulations or by fitting to the nominal diffusion coefficients in the materials system. To account for the environment dependence of the activation barrier, we used the Final-Initial-System-Energy (FISE) method [45] to update the activation barrier for each KMC event based on the local atomic configurations. In the FISE method, the effective activation barrier is given by

$$E^m = E_0 + (E_f - E_i)/2 \tag{18}$$

In the equation E_0 is a constant, usually the activation barrier in the pure metallic matrix. E_f and E_i represent the final and initial system energies calculated by the broken bond mode:

$$E_{total} = \sum_{\phi} (\sum_{i,j} \varepsilon_{X-Y}^{\phi}) \tag{19}$$

Here ε_{X-Y}^{ϕ} means the bond energy between elements X and Y in the phase ϕ, e.g, fcc or bcc phases. The bond interactions are defined on nearest-neighbor (NN) atoms of different orders, depending on the complexity of the system. In our AKMC model, both the first-NN and second-NN interactions are included. The bond energies, as defined in Vincent et al. [46], are fitted to many relevant materials properties obtained from experiments or DFT calculations, including the cohesive energy and vacancy formation energy in bcc-Fe, heat of solution of alloy elements in bcc-Fe, and the binding energies between solute atoms and point-defects, e.g., vacancy-vacancy, vacancy-Cu and Cu-Cu.

To simulate systems other than perfect bcc lattice, for example, with defects, sink and source mechanisms are also introduced for vacancies in our current implementation of the AKMC model. Once a vacancy reaches a sink, it will transform into the matrix element. The types of sinks added include 1D (dislocations or loops), 2D (interfaces), and 3D (spherical) entities. The source term is added as a reaction that converts element A to element B, with an input thermal barrier and a target number of element B. The reaction is turned on if the current number of element B is below target, and off if it's beyond. The reaction takes place only at specified lattice sites representing the sources. The sink and source functions are demonstrated using a simulation cell of 144,000 atoms with no vacancies initially in Figure 18. A sink of octagon in shape is added with the sink radius of 2.0 a_0, where a_0 is the lattice constant. Lattice sites not included in the sink region are assigned as vacancy sources to maintain a vacancy number of 200 during the simulation. The simulation runs for 10000 KMC steps at the temperature of 0.2 eV. The sink mechanism is turned on when the number of vacancy is below the target, and the source mechanism is turned on when it is beyond. As shown in Figure 18 (a), the number of vacancies quickly reaches to 200 after the simulation starts. Due to the introduction of the sink, vacancies were absorbed by the sink with a constant rate. However, the number of vacancy remained as almost constant (200) by the sink/source mechanisms during the course of the simulation. The small fluctuations seen are owing to the on/off reaction events. Both the current vacancies and those absorbed at the sink are shown in Figure 18 (b). The current vacancies are randomly distributed with a few clusters. The absorbed vacancies depict the shape of the sink.

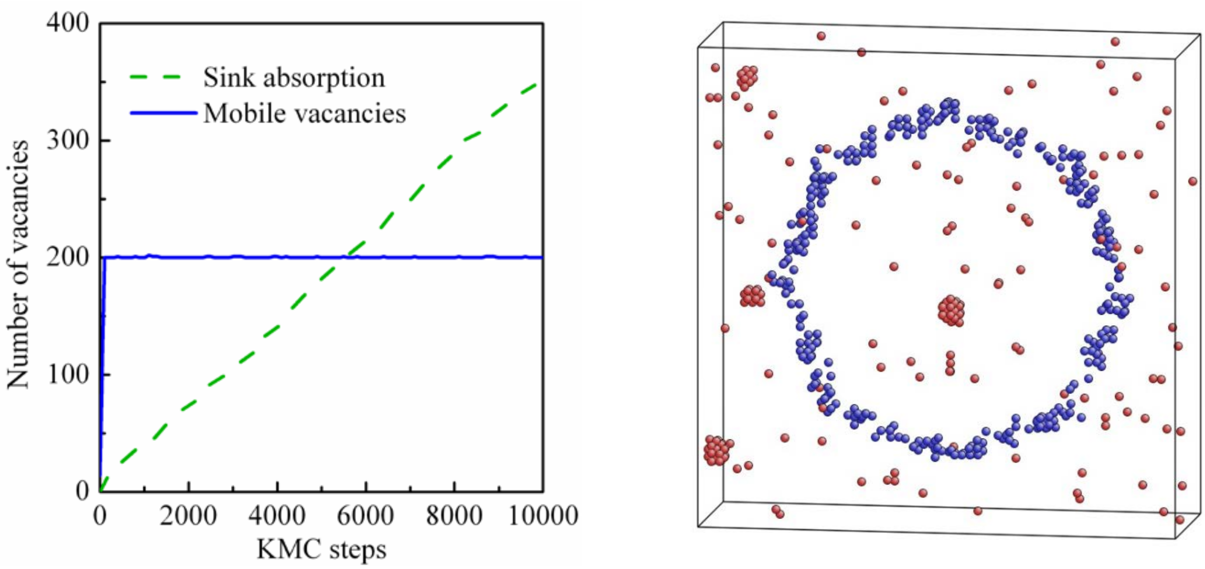

Figure 18: (a) number of mobile and absorbed vacancies as functions of KMC steps; (b) atomic configuration at 10000 KMC step. Blue atoms represent vacancies absorbed by the sink and red atoms represent currently mobile ones in the system.

In addition to the sink and source mechanisms, the elastic interactions between solute atoms and dislocations and defect loops are also incorporated into the current AKMC model. As will be shown later, the elastic interaction is a dominant factor for the interaction between dislocation (loops) and solute atoms, and it can be well described using the linear-elastic theory. This interaction is given by $E^b = P\Delta V$ [47]; here P is the pressure and ΔV is the size mismatch, i.e., the volumetric change induced by replacing a matrix atom with a substitutional solute atom. Positive pressure means tension and negative means compression. Therefore, oversize solute atom such as Cu will be attracted at the tensile regions and repelled at the compressive regions. In our AKMC model, the pressure P due to presence of lattice defects (i.e. dislocations, vacancy and self interstitial, SIA loops) is numerically computed using the Stroh formalism in linear-elastic theory [48]. In the calculations, we use cubic symmetry for bcc-Fe. The elastic moduli were taken as c11 = 243 GPa, c12 = 143.5 GPa and c44 = 116 GPa. As shown in Figure 19, the pressure given by the Stroh formalism agrees very well with that calculated by the MD simulations using the Mendelev potential [38]. As will be shown later, the long-range elastic interaction will affect the precipitation of Cu both kinetically and thermodynamically.

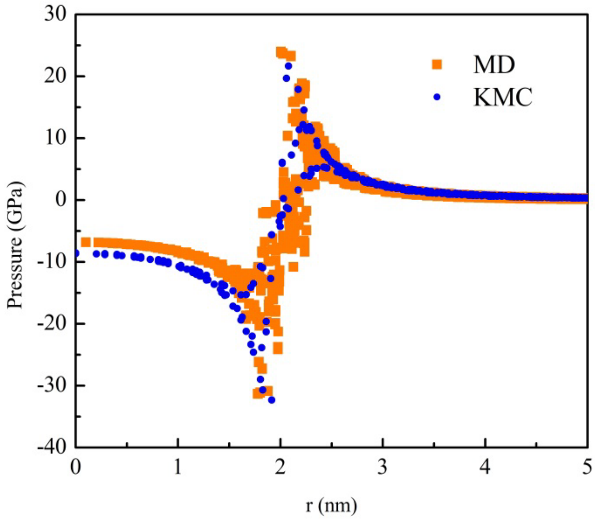

Figure 19: Atomic stress as a function of vacancy loop radius from MD and KMC (Stroh formalism) calculation for a spherical SIA loop. The loop radius is 2.0 nm

4.3 Results and Discussion

4.3.1 Segregation energies from MD simulations

In this section, the interaction between Cu and lattice defects will be elucidated by calculating the interaction energies using MD simulations. The lattice defects considered in this study include point-defects, edge and screw dislocations, SIA and vacancy loops and void. For point defects, the binding energy is defined as the energy required to dissociate the two defects. For other extended defects, the segregation energy is defined as the difference in energy of a solute atom occupying a segregation site with that of a regular solute. The binding energy can be taken as the segregation energy with the opposite sign. Therefore, positive binding (negative segregation) energy represents attraction, and negative binding (positive segregation) energy represents repulsion.

4.3.1.1 *Cu/Point-defects interaction*

The interactions of Cu with a point-defect or another Cu atom were found to be short range within about 2 a_0. As shown in Fig.3, a Cu atom is attracted by a vacancy, V, or another Cu atom. The maximum binding energies for Cu-V and Cu-Cu were found to be about 0.10 and 0.08 eV respectively at the first nearest neighbor (1NN) distance. In contrast, the Cu-SIA interaction was found to be repulsive. The strongest repulsion was obtained with Cu being one of the split dumbbell atoms. Due to the attractive interaction between Cu atoms, a strong precipitation tendency of Cu is expected in bcc-Fe, in accordance to the very low solubility. These results are shown in Figure 20, and are in good agreement with previous DFT calculations [49]. The results indicate that, while under radiation, Cu atoms prefer to cluster with vacancies, leading to enhanced diffusion and nucleation of precipitates. On the other hand, SIAs will have less effect on Cu diffusion and precipitation. It is also expected that they will recombine with vacancies and affect the overall vacancy concentration.

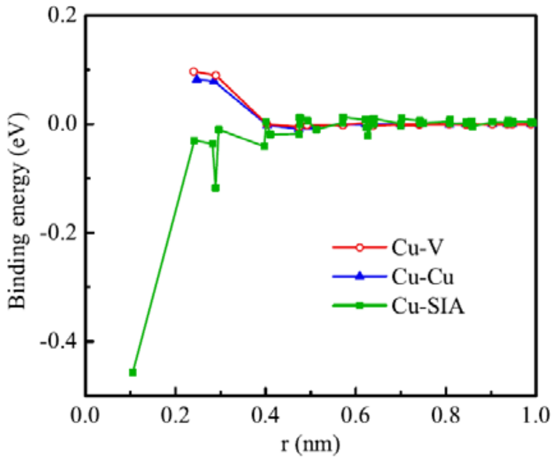

Figure 20: Binding energies of a Cu solute atom with a point defect or another Cu solute atom, as functions of distance.

4.3.1.2 The role of dislocations

The dislocations considered here were straight with infinite length with pure edge or screw characters. The Burgers vectors were taken as ½<111> for both. Unlike point defects for which the interactions with solute atom are usually short range, dislocations may interact with solute atoms in long range through the associated stress-fields. For edge dislocation, non-zero hydrostatic pressure present even at the long range with both tensile and compressive regions. As shown in Figure 21(a), Cu is attracted by the tensile region (below the core) and is repelled by the compressive region (above the core). The absolute interaction energy decreases with increasing distance from the core; however, as can be seen, interaction energy is still not zero even at much longer distance. On the other hand, for screw dislocation, the interaction is short range within the core region, owing to the zero hydrostatic pressure resulting from the pure shear displacement field of screw dislocations. Cu is attracted at the core of screw dislocation, with a much weaker interaction than that for the edge dislocation.

The different results exhibited by edge and screw dislocations suggested that the solute interactions might be classified into the long-range interaction induced by the stress-field and short-range interaction from the dislocation core-effect. The elastic interaction can be described as $E^b = P\Delta V$ [47]. The pressure P can be calculated using the linear-elastic theory, e.g., using the Stroh formalism. The size mismatch ΔV can be obtained using MD simulations. In order to get the size mismatch of Cu in bcc-Fe, a few MD simulations were carried out in the present work, with the Cu concentration ranging from 0.0 to 10.0 atomic percent. Cu atoms were randomly inserted as substitutions. By determining the lattice constant, the average atomic volume V was obtained as a function of Cu concentration C_{Cu}. As shown in Figure 21(b), V increases proportionally with C_{Cu}. A linear fitting gives $V(C_{Cu})=V_0+C_{Cu}\Delta V= V_0(1+ 0.026C_{Cu})$; here V_0 is the atomic volume for bcc-Fe without Cu and it is 11.64Å^3. Correspondingly, the size mismatch is determined to be as $\Delta V =0.026V_0$.

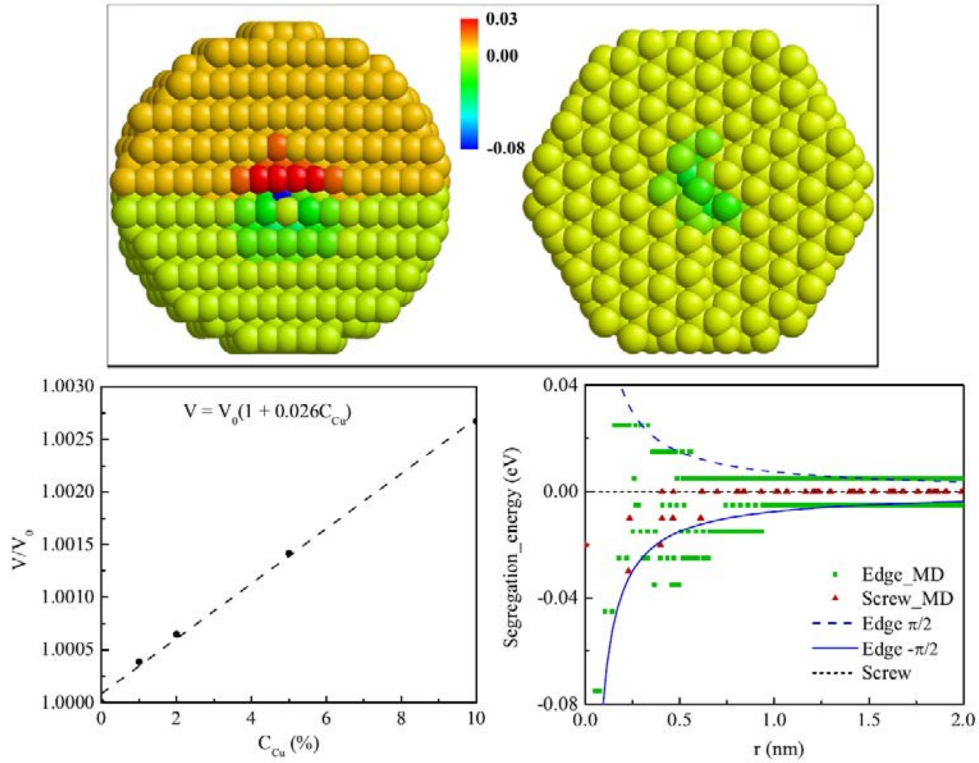

Figure 21: (a) Atomic configurations of an edge (left) and a screw (right) dislocation, with the atoms colored by segregation energies, (b) Lattice constant of bcc Fe as a function of Cu concentration, and (c) the segregation energies of Cu near an edge and a screw dislocation as functions of distances from the dislocation core. The solid and dash curves represent the linear-elastic estimation.

In Figure 21(c) the segregation energies calculated from MD simulations are compared with the elastic interactions obtained from the linear-elastic theory. For screw dislocation, the elastic interaction is zero everywhere and the interaction is dominated by the core effect in the short-range. For edge dislocation, the elastic interaction varies with locations, with the maximum attraction along the $\theta=-\pi/2$ and maximum repulsion along the $\theta=\pi/2$ directions. Here θ is the angle between the Burgers vector and the vector pointing from the dislocation core to the segregation site, projected onto the plane normal to the dislocation line-vector. The interaction is long-range with non-zero interaction energy at places far from the core. It is also interesting to notice that the results from MD calculations agree well with the linear-elastic estimation, suggesting that the latter is the dominant effect. Indeed, the much weaker interaction energy given by screw dislocation indicates that the core-effect is less significant compared to the elastic effect. This conclusion is very important for the AKMC simulations where the core-effect is not included owing to the rigid-lattice assumption. The results also shows that the dominant long-range elastic interactions can be efficiently included into AKMC simulations by introducing a stress field given by the linear-elastic theory, as has been described in Section 1.2.3.

4.3.1.3 The effects of defect loops

Dislocation loops have been widely observed in neutron radiated bcc-Fe or Fe-based alloys. According to experimental observations, the loops may have either ½<111> or <100> burgers vector, residing on {111} or {100} crystallographic planes respectively [50]. In the following, only the results for {100} loops will be summarized. All loops considered here are assumed to be in circular in shape.

For defect loops, the strongest interaction with Cu is exhibited near the loop edges (Figure 22(a)), which are the dislocation lines (cores) if we consider the defect loops as analogues of dislocations of pure edge character. The interaction energies change sign across the loop edge. For SIA loops, Cu was found to be attracted to the outside of the loops and repelled from inside the loops. The opposite trend was observed for vacancy loops. For the SIA loop of 2.0 nm, the interaction is dominated by repulsion, and it is dominated by attraction for the 2.0 nm vacancy loop, suggesting that with the same size, vacancy loops are stronger sinks for Cu. The interaction between Cu and defect loops also exhibited some size dependence. By increasing the SIA loop size from 2.0 nm to 10.0 nm, the repulsion inside the loop decreases but the attraction outside the loop increases, indicating that for SIA loops Cu may prefer to precipitate at larger ones.

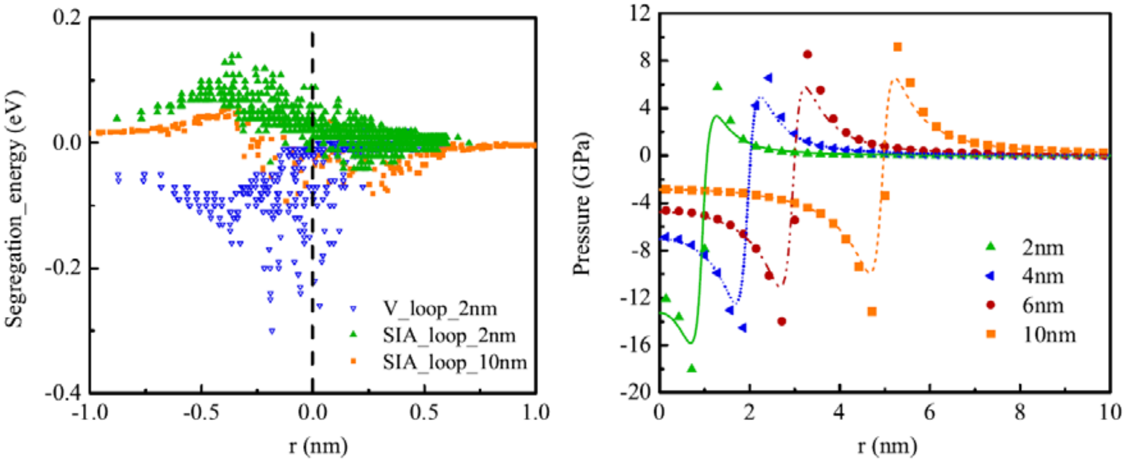

Figure 22: (a) Cu segregation energies as functions of distances from the edges of vacancy (V_loop) and SIA loops (SIA_loop) and (b) the hydrostatic pressure for SIA loops of different sizes. Symbols represent MD results and the curves are from Stroh formalism.

As has been shown in Section 1.3.1.2, the interaction between Cu and pure edge dislocation is dominated by the elastic effect. With pure edge character, similar dominant elastic interaction is expected for defect loops. Therefore, it will be helpful to interpret the results in Figure 22(a) with the information on the associated stress-fields. In Figure 22(b), the pressures of SIA loops with the diameter from 2.0 to 10.0 nm are plotted. Again the MD results are found to be in good agreement with those from Stroh formalism. It is shown that for SIA loops, the pressure is compressive inside the loop and tensile outside, in accordance with repulsion and attraction to Cu shown in Figure 22(a). Also, as the size increases, the compression decreases and the tension increases, leading to the size dependence in the segregation energy of Cu. Furthermore, for a SIA loop with fixed size, the maximum compression inside the loop is higher than the maximum tension outside, indicating elastically stronger maximum repulsion than maximum attraction. While for vacancy loops, the stress fields are exactly the opposites of SIA loops of the same size. With the same size, the maximum attraction inside a vacancy loop is stronger than the maximum attraction outside a SIA loop. Therefore, vacancy loops are stronger sinks for Cu than SIA loops when the sizes are similar. As the sizes approach infinite, both vacancy and SIA loops resemble pure edge dislocation with infinite length.

The results for ½<111> loops are similar to those shown for <100> loops of the same size and nature, but with smaller absolute values owing to the smaller Burgers vector.

4.3.1.4 The role of voids

Due to low solubility of Cu in bcc-Fe, void surfaces are expected to be preferential precipitation sites. Indeed, MD calculations show that the binding energy of Cu at the surface of a 1.0 nm void can be as high as 0.75 eV, as shown in Figure 23. The interaction between Cu and voids is attractive and short-range within about one a_0, followed by a slightly repulsive zone. Compared to other types of extended defects considered, voids are found to be the strongest sinks, indicated by the segregation energies plotted in Figure 23. Following voids, vacancy loops are shown stronger sinks than edge dislocation and the SIA loops. To summarize, vacancy type of defects are in general stronger sinks for Cu, which is oversize in bcc-Fe, than SIA type of defects. For defect with non-zero stress field, long-range elastic interaction presents and it dominates the interaction with Cu. For other defects, the interaction is short-range, usually within a couple of lattice constant.

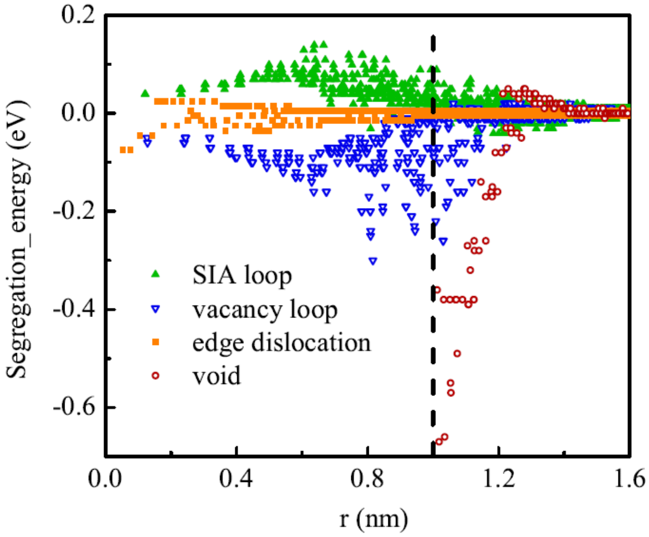

Figure 23: Cu segregation energies at different lattice defects including edge dislocation, defect loops and void. The dash line shows the edges of defect loops and the void surface.

4.3.2 Heterogeneous precipitation from MMC simulations

The above results on segregation energies of all extended defects considered here indicate that they can be preferential precipitation site of Cu. It is therefore of an interest to explore the precipitation morphology. Owing to the slow kinetics involved, we used MMC instead of MD to investigate the Cu precipitation behavior. For all MMC simulations, the Cu concentration of 1.0 atomic percent was used. This concentration is higher than in typical RPV steels, however, it was used in here in order to accelerate the precipitation process for the computational efficiency. In MMC simulations, both the translation and swap moves described earlier were performed. The translation move was used to relax the defect configuration. The swap move can be regarded as the diffusion of Cu. It searches randomly in the configuration space and evolve the system downhill in the potential energy. For all the MMC simulations were carried out for

5 million MC steps; however, in none of the simulations the final thermal equilibrium was reached. Nevertheless, the results obtained are sufficient enough to show the precipitation tendency.

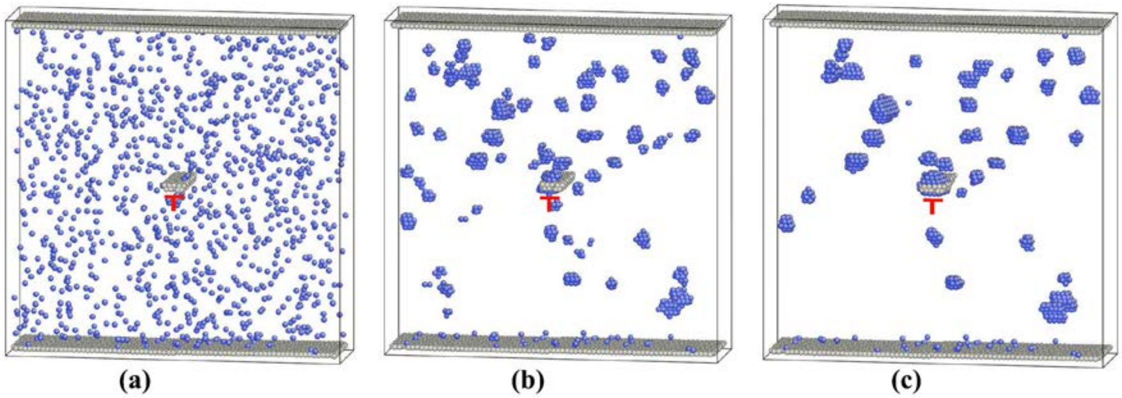

Figure 24: Atomic configurations to demonstrate the Cu precipitation around an edge dislocation at (a) 0, (b) 2.5 million and (C) 5 million MMC steps. Cu atoms are show in blue and non-BCC Fe atoms in gray spheres which indicate the dislocation and the constrained layers at the top and the bottom of the simulation cell.

In Figure 24, the MMC simulation results for an edge dislocation are summarized. Due to the non-periodic boundary conditions at the top and bottom surfaces, two fixed layers 1.0 nm each in thickness, no MMC moves were performed. The simulation cell contained xx atoms. Initially all Cu atoms were randomly distributed, and excluding those in the fixed layers, they form clusters in 2.5 million MMC steps as shown in Figure 24(a) and (b). Due to the repulsion in the compressive region (below the dislocation line), more Cu clusters (precipitates) were observed in the tensile region (above the dislocation line). Only one precipitate was found attached to the dislocation core. With more MMC steps, some small clusters dissolved and some relatively large ones kept growing in size by absorbing Cu atoms dissolved from the smaller ones, showing an Oswald-ripening behavior; Figure 24(b) and (c). We note that in the MMC simulations the coalescence of clusters is suppressed since the diffusion of Cu atoms takes place primarily by the swap move, which enhances the dissociation of Cu atoms from the clusters. The Cu clusters tend to develop a {110} faceting while growing in size which has also been observed in previous studies in the literature.

Similar to edge dislocation, the precipitation of Cu around SIA loops is also influenced by the stress-field. To study the size effect, two <100> SIA loops having diameters of 2.0 nm and 10.0 nm were simulated. For the 2.0 nm SIA loop, all precipitates were found to form in the matrix, without the segregation/precipitation near the loop edges, Figure 25(a) and (c). This is because the interaction with Cu is dominated by repulsion, as shown earlier in Figure 22(a). While for the 10.0 nm loop, clear precipitation of Cu with the non-bcc Cu atoms was observed at the loop edges (Figure 25(d)-(f)). The local Cu concentration near the loop edge was much higher than the average concentration of 1.0 atomic percent, indicating heterogeneous precipitation at SIA loops that are larger in size.

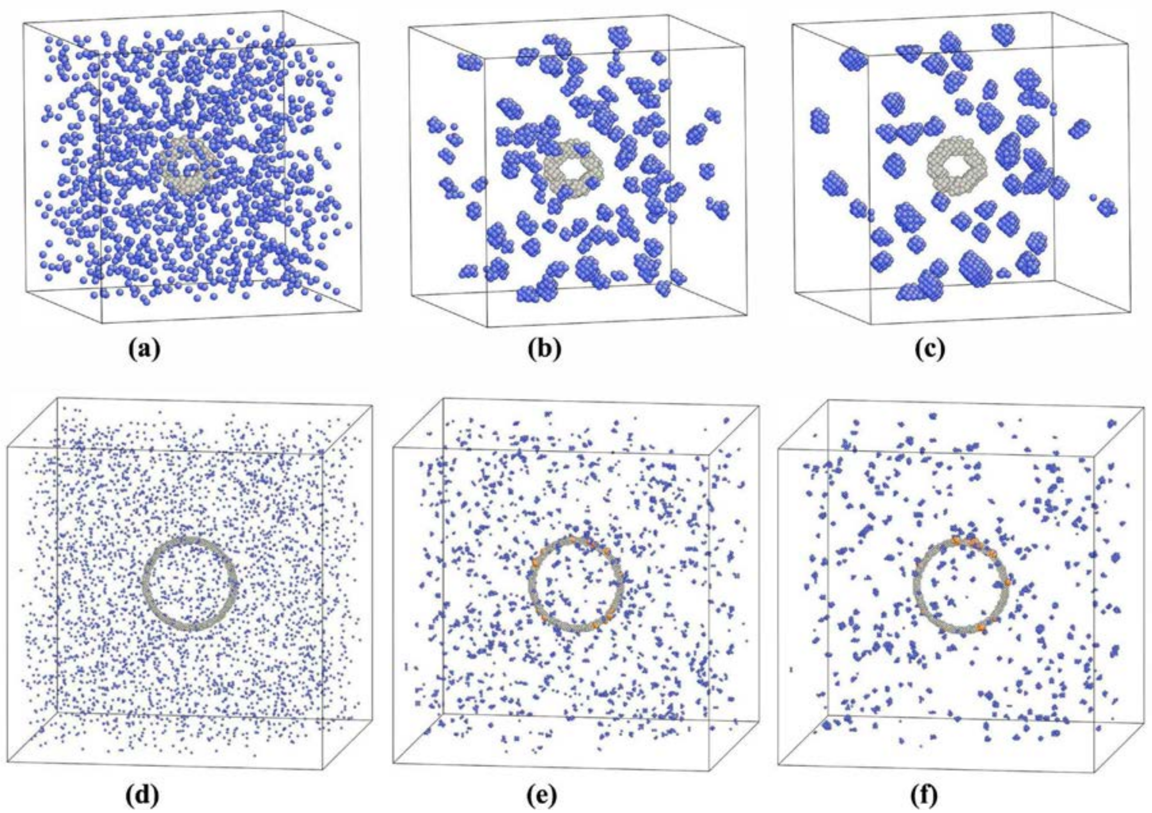

Figure 25: Atomic configurations to demonstrate the Cu precipitation around a 2.0 nm SIA loop at (a) 0, (b) 2.5 million and (c) 5 million MMC steps; and those for a 10.0 nm at (d) 0, (e) 2.5 million and (f) 5 million MMC steps. bcc-Cu atoms are show in blue; non-bcc Cu atoms are shown in yellow; and non-bcc Fe atoms (indicating SIA loops) are shown in gray spheres.

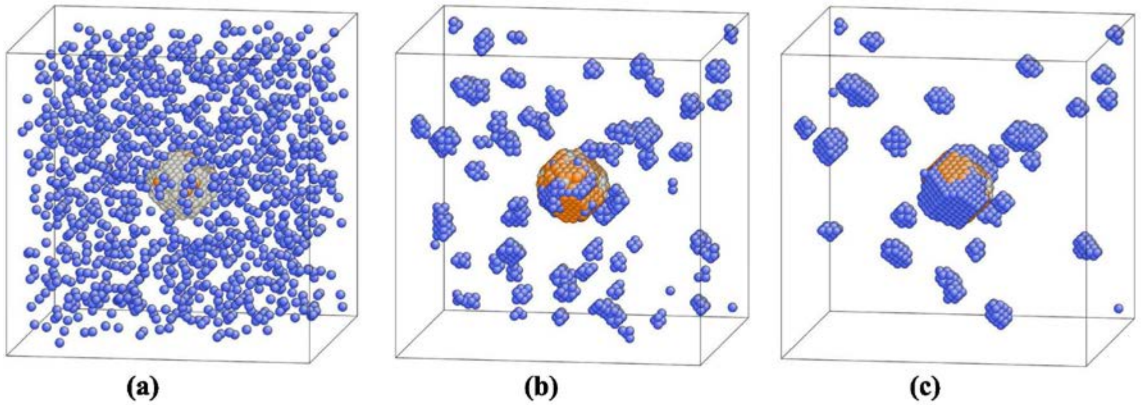

Figure 26: Atomic configurations to demonstrate the Cu precipitation around a 2.0 nm void at (a) 0, (b) 2.5 million and (c) 5 million MMC steps. bcc Cu atoms are show in blue; non-bcc Cu atoms are shown in yellow; and non-bcc Fe atoms (indicating the void) are shown in gray spheres.

Due to the high segregation energy, strong precipitation tendency was observed for voids. As shown in Figure 26, the surface of a 2.0 nm void was almost all covered by Cu atoms in 2.5 million MMC steps. After 5 million MMC steps, the spherical void developed into a {110} faceted precipitates. Oswald-ripening type behavior was also observed, with the small clusters dissolving and large ones growing in size. The precipitate formed at the void surface contained many more Cu atoms that in any other cluster, indicating strong heterogeneous precipitation behavior.

In general, the results obtained from the MMC simulations on the precipitation behavior are in agreement with the MD results on segregation energies. Heterogeneous precipitation was observed at locations with negative segregation energies, such as the exterior of the SIA loops with relatively large size and the surfaces of voids. The MMC results obtained from an empirical potential can be good validations for the results obtained from the AKMC simulations, where the defect configurations are not fully represented (i.e. dislocation cores) due to the rigid-lattice assumption, and also less accurate pair-wise interactions are used to describe the system.

4.3.3 Precipitation kinetics from AKMC simulations

Using our AKMC model described in Section 2.3, the precipitation kinetics of Cu and the effects of edge dislocation and defect loops were investigated. In the AKMC simulations, periodic simulations cells with 2 million atoms were used, with the composition of Fe-1.34%Cu. In each simulation, one vacancy was introduced into the system, giving a nominal vacancy concentration of C_v of 5×10^{-7}. The simulation temperature was 773K, at which the thermal equilibrium vacancy concentration is given by $C^{eq} \sim \exp(-E^f/KT) = 1.3\times10^{-12}$. For comparison, several parallel AKMC simulations are carried out for the following cases: (1) in addition to Cu, 1%Ni and 1.5%Mn, (2) a vacancy loop of 2.8 nm in radius, (3) a SIA loop of 2.8nm in radius, and (4) an infinitely long edge dislocation. The loops and dislocations were represented by their corresponding elastic stress-fields and they remained stationary during the course of the simulations.

To elucidate the kinetics, the volumetric density and average size of Cu precipitates are plotted in Figure 27. To be consistent with previous modeling and experimental studies in the literature, here we also considered Cu clusters with 10 or more Cu atoms as precipitates. Compared to the only Cu being the alloying element, introduction of other alloying elements such as Ni and Mn was found to delay the precipitation kinetics, in terms of both reduced density and average size of the precipitated. It has been shown in previous AKMC study that the presence of Ni enhances the nucleation but impedes the growth of Cu clusters [51]. Indeed, if we consider all Cu clusters with 2 or more Cu atoms, the density was higher for the Cu-Ni-Mn case than that for Cu only. Ni and Mn require higher activation barriers and are less mobile than Cu. They are also attractive to Cu and act as nucleation sites for Cu precipitates, enhancing the nucleation. Meanwhile, clustering with Ni and Mn reduces the effective mobility of Cu atoms, delaying further growth of small Cu clusters via diffusion of Cu atoms. As a result, both the density and average size of Cu precipitates (10 or more Cu atoms) are reduced by the presence of Ni and Mn, as shown in Figure 27.

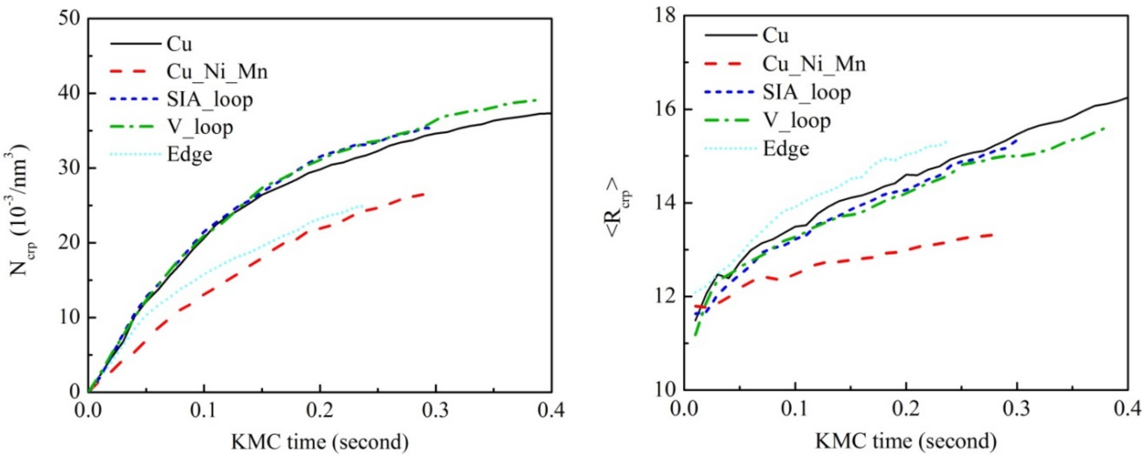

Figure 27: (a) Volumetric density (N_{crp}) and (b) average size (<R_{crp}>) of CRPs as functions of KMC time.

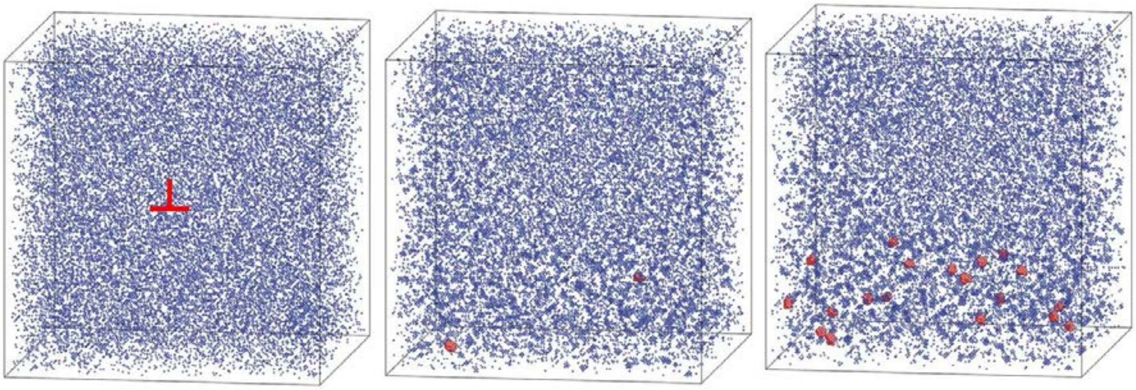

Figure 28: Atomic configurations of the system with an edge dislocation at (a) 0, (b) 0.03 and (c) 0.07 seconds in KMC time. Cu clusters with 20 or more atoms are shown in red and other Cu atoms in blue. Fe atoms are omitted for clarity. The position of the dislocation core is shown in (a).

The presence of edge dislocation may also reduce the density of Cu precipitates. However, the average size was found to be larger than that for the Cu only case, as shown in Figure 27(b). Due to the associated stress-field, the nucleation and growth of Cu precipitates are suppressed in the compressive region, but on the other hand, enhanced in the tensile region. As shown in Figure 28(a) to (c), the sizes of Cu clusters below the dislocation (tensile region) are much larger than those seen at the above (compressive region) of the dislocation line. At the time of 0.07 second (KMC time), all precipitates with 10 or more Cu atoms formed are below the dislocation line, with none above. The overall effect of edge dislocation results in reduced precipitate density and increased average size. Also, the distribution of precipitates shown in Figure 28 from AKMC simulations is consistent with the results from MMC simulations shown earlier in Figure 24.

In contrast, the effects of SIA and vacancy loops are less significant than those for edge dislocation, probably due to the relatively small size of the loops considered in here. For vacancy and SIA loops, similar effects are observed. Compared to the case of Cu only, introduction of defect loops leads to slight decrease in precipitate density, but slight increase in average size. Further study on the size effect is required to fully understand the effect of these defect loops.

4.4 Precipitation Kinetics and Aging Modeling Summary

For the first year of the effort to model the late blooming phases and precipitation kinetics in RPV steels our efforts concentrated on the understanding of the atomic scale events which will be the foundations for mesoscale and continuum level modeling and simulations.

In this work, we have used MD simulations to elucidate the interaction between Cu and lattice defects including point defects, dislocations, loops and voids, and used MMC simulations to explore the possible heterogeneous precipitation behavior. Two types of interactions, short-range interaction and long-range elastic interaction have been identified. The elastic interaction was found to be a dominant effect for dislocations and defect loops.

Based on the results from MD and MMC simulations, an AKMC model has been developed. On the basis of a conventional AKMC model, sink/source mechanisms and elastic interaction are included to allow for heterogeneous precipitations at the extended defects.

Preliminary results of AKMC simulations show that alloy elements and lattice defects such as dislocation and defect loops significantly affect the evolution kinetics of CRPs which has not been considered in the previous studies available in the literature.

5. Summary

During FY-2013 we have made progress in three areas as detailed in this report:

At the engineering scale, code benchmarking has been performed to provide confidence in Grizzly's prediction of the global coupled thermal and mechanical response of a reactor pressure vessel subjected pressurized thermal shock loading conditions, including the effects of a stainless steel liner. In addition, progress has been made toward developing a 3D fracture mechanics assessment capability in Grizzly. A submodeling approach for embedding detailed models of the material in the vicinity of an arbitrarily oriented flaw has been developed and demonstrated. Progress has been made toward developing a *J*-integral evaluation capability within Grizzly, and this currently limited capability has been demonstrated and verified on a simplified 2D benchmark problem. These developments, when completed in the next fiscal year, will enable Grizzly to perform detailed fracture assessments of arbitrary 3D flaws in embrittled reactor pressure vessels.

At the fracture test scale, two different approaches have been pursued to estimate ductile brittle fracture transition (DBT) and the resulting master curve. The first approach has been reported extensively in the literature. Although first approach has been successful to capture DBT; however, the effect of microstructure on crack growth cannot be incorporated using this method. Also, the usability of this method at engineering scale is somewhat restricted where the material properties and stress-states vary considerably. Moreover, it is computationally inefficient, requiring extensive post-processing after the simulations. To alleviate these issues, a cohesive zone based approach has been proposed in the present work. A unified constitutive model capturing both ductile and brittle modes of crack growth has been developed and the results obtained from the simulations were validated with the available data from the literature. The model enables the simulation of explicit crack growth at both stable and unstable regimes of fracture. Also it provides the ability to incorporate more physical lower scale models based on the underlying microstructures. Such a multiscale approach will significantly improve the predictive capabilities of the current models, which are still largely empirical.

At the atomistic scale, an Atomistic Kinetic Monte Carlo (AKMC) model has been developed for Fe-Cu-Mn-Ni-Si system, which was the primary objective for FY2013. Furthermore, the effect of neutron radiation was incorporated by considering the interaction between the alloying elements and radiation-induced lattice defects. Focusing on Cu, we used molecular dynamics (MD) simulations to elucidate their interactions with several lattice defects including point-defects, dislocations, voids and defect loops. It was found that the interaction can be classified into long-range interaction associated with the stress-fields from dislocations and loops, and short-range interaction with point defects and voids. The long-range interaction can be described well using linear-elastic theory. The results on the interaction energies are in good agreement with the precipitation morphology predicted by Metropolis Monte Carlo (MMC) simulations. Based on the MD results and literature data, an AKMC model was developed at INL with the short-range interactions represented by pair-wise bonds between nearest neighbors and the long-range interaction by linear-elastic theory. Some preliminary AKMC results showed that the introducing of alloying elements and lattice defect has important effects on the formation of Cu-rich-precipitates which has not been taken account previously in the available literature.

6. References

1. E.D. Eason, G.R. Odette, R.K. Nanstad, T. Yamamoto, A Physically Based Correlation of Irradiation-Induced Transition Temperature Shifts for RPV Steels, ORNL/TM-2006/530, Oak Ridge National Laboratory, 2007.
2. E.D. Eason, G.R. Odette, R.K. Nanstad, T. Yamamoto, A physically-based correlation of irradiation-induced transition temperature shifts for RPV steels, Journal of Nuclear Materials 433(2013)240-254.
3. T. L. Dickson, P.T. Williams, S. Yin, Fracture Analysis of Vessels – Oak Ridge FAVOR, v09.1, Computer Code: User's Guide, ORNL/TM-2010/4, Oak Ridge National Laboratory, December 2009.
4. B. Healy, A. Gullerud, K. Koppenhoefer, A. Roy, S. RoyChowdhury, M. Walters, B. Bichon, K. Cochran, J. Sobotka, M. Messner, R. Dodds, WARP3D-Release 17.3.1, 3-D Dynamic Nonlinear Fracture Analysis of Solids Using Parallel Computers, UILU-ENG-95-2012, University of Illinois at Urabana-Champaign, September, 2012.
5. Rice, J. R., "A Path Independent Integral and the Approximate Analysis of Stress Concentration by Notches and Cracks." *Journal of Applied Mechanics* 35(1968): 379-386.
6. Li, F. Z., C. F. Shih, and A. Needleman. "A Comparison of Methods for Calculating Energy Release Rates." *Engineering Fracture Mechanics* 21(1985): 405-421.
7. Eshelby, J. D., "Energy Relations and the Energy-Momentum Tensor in Continuum Mechanics." *Inelastic Behavior of Solids* New York: McGraw-Hill, 1970.
8. National Agency for Finite Element Methods and Standards (U.K.): Test 1.1 from NAFEMS publication "2D Test Cases in Linear Elastic Fracture Mechanics, " R0020.
9. J. F. Knott, "Micromechanisms of fracture and the fracture toughness of engineering alloys," *Fracture*, vol. 1, pp. 61-91, 1977.
10. C. J. Jr. McMahon and M. Cohen, "Initiation of cleavage in polycrystalline iron," *Acta. Metal.*, vol. 13, pp. 591-604, 1965.
11. E. Smith, "The nucleation and growth of cleavage microcracks in mild steel," in *Proceedings of the Conference on the Physical Basis of Yield and Fracture*, London, 36-46, p. 1966.
12. R. O. Ritchie, J. F. Knott, and J. R. Rice, "On the relationship between critical tensile stress and fracture toughness in mild steel," *J. Mech. Phys. Solids*, vol. 21, pp. 395-410, 1973.
13. D. A. Curry and J. F. Knott, "Effect of microstructure on cleavage fracture toughness in mild steel," *Metal Science*, vol. 13, pp. 341-345, 1979.
14. F. M. Beremin, "A local criterion for cleavage fracture of a nuclear pressure vessel steel," *Met. Trans. A*, vol. 14A, pp. 2277-2287, 1983.
15. W. Weibull, "A statistical distribution function of wide applicability," *Jour. App. Mech.*, vol. 18, pp. 293-297, 1953.
16. G. Rousselier, "Ductile fracture models and their potential in local approach of fracture," *Nuc. Engg. Des.*, vol. 105, pp. 97-111, 1987.
17. A. L. Gurson, "Continuum theory of ductile rupture by void nucleation and growth: Part I-yield criteria and flow rules for porous ductile media," *Trans. ASME, Jour. Engg. Mat.*, vol. 99, pp. 2-15, 1977.
18. B. Tanguy, J. Besson, R. Piques, and A. Pineau, "Ductile to brittle transition of an A508 steel characterized by Charpy impact test. Part I: experimental results," *Engg, Frac. Mech.*, vol. 72, pp. 49-72, 2005.

19. B. Tanguy, J. Besson, R. Piques, and A. Pineau, "Ductile to brittle transition of an A508 steel characterized by Charpy impact test. Part II: modeling of the Charpy transition curve," *Engg. Frac. Mech.*, vol. 72, pp. 413-434, 2005.
20. M. K. Samal, M. Seidenfuss, E. Roos, B. K. Dutta, and H. S. Kushwaha, "Experimental and numerical investigation of ductile-to-brittle transition in a pressure vessel steel," *Mat. Sc. Engg. A*, vol. 496, pp. 25-35, 2008.
21. M. K. Samal, M. Seidenfuss, E. Roos, B. K., Dutta, and H. S. Kushwaha, "Finite element formulation of a new nonlocal damage model," *Finite Elem. Ana. Des.*, vol. 44, pp. 358-371, 2008.
22. B. Z. Margolin, V. A. Shvetsova, A. G. Gulenko, and V. I. Kostylev, "Application of a new cleavage fracture criterion for fracture toughness prediction for RPV steels," *Fatigue Fract. Engg. Mat. Struct.*, vol. 29, pp. 697-713, 2006.
23. L. Vincent, M. Libert, B. Marini, and C. Rey, "Towards a modelling of RPV steel brittle fracture using crystal plasticity computations on polycrystalline aggregates," *Jour. Nuc. Mat.*, vol. 406, pp. 91-96, 2010.
24. I. Scheider and W. Brocks, "Simulation of cup-cone fracture using the cohesive model," *Engg. Frac. Mech.*, vol. 70, pp. 1943-61, 2003.
25. T. L. Anderson, *Fracture Mechanics*, 2nd ed. New York, USA: CRC Press, 1994.
26. M. Anvari, I. Scheider, and C. Thaulow, "Simulation of dynamic ductile crack growth using strain rate and triaxiality-dependent cohesive elements," *Engg. Frac. Mech.*, vol. 73, pp. 2210-2228, 2006.
27. Y. F. Gao and A. F. Bower, "A simple technique for avoiding convergence problems in finite element simulations of crack nucleation and growth on cohesive interfaces," *Modelling Simul. Mat. Sci. Engg.*, vol. 12, pp. 453-463, 2004.
28. V. Tvergaard and A. Needleman, "Analysis of the cup-cone fracture in a round tensile bar," *Acta. metall.*, vol. 32, no. 1, pp. 157-169, 1984.
29. V. Tvergaard and J. W. Hutchinson, "The relation between crack growth resitance and fracture process parameters in elastic-plastic solids," *J. Mech. Phys. Solids*, vol. 40, pp. 1377-1397, 1992.
30. U.S. Nuclear Regulatory Commission, Radiation Embrittlement of Reactor Vessel Materials, Regulatory Guide 1.99 Revision 2, Washington, DC, 1988.
31. S.J. Zinkle and G.S. Was, Acta Mater. 61 (2013) 735–758.
32. G.R. Odette and R.K. Nanstad, JOM 61 (2009) 17–23.
33. Y. U. Heo, Y. K. Kim, J. S. Kim, J. K. Kim, Acta Mater. 61 (2013) 519–528.
34. B. Radiget, A. Barbu and P. Pareige, J. Nucl. Mater. 360, (2007) 104-107.
35. E. Meslin, M. Lambrecht, M. Hernández-Mayoral, F. Bergner, L. Malerba, P. Pareige,B. Radiguet, A. Barbu, D. Gómez-Briceño, A. Ulbricht and A. Almazouzi, J. Nucl. Mater. 406 (2010) 73.
36. S. Plimpton, J Comp Phys, 117 (1995) 1-19.
37. G. Bonny, R.C. Pasianot, N. Castin, and L. Malerba, Phil. Mag. 89, (2009) 3531-3546.
38. M.I. Mendelev, A. Han, D.J. Srolovitz, G.J. Ackland, D.Y. Sun and M. Asta, Phil. Mag. A 83 (2003) 3977.
39. Y. Mishin, M.J. Mehl, D.A. Papaconstantopoulos, A.F. Voter and J.D. Kress, Phys. Rev. B 63 (2001) 224106.
40. A.F. Voter and S.P. Chen, Mater. Res. Soc. Symp. Proc. 82 (1987) 175.
41. R.C. Pasianot and L. Malerba, J. Nucl. Mater. 360 (2007) 118.
42. G. Bonny, R.C. Pasianot and L. Malerba, Model. Simul. Mater. Sci. Eng. 17 (2009) 025010.
43. D. Terentyev, X. He, E. Zhurkin and A. Bakaev, J. Nucl. Mater. 408 (2011) 161–170
44. Crossing the Mesoscale No-Man's Land via Parallel Kinetic Monte Carlo, S. Plimpton, C. Battaile, M. Chandross, L. Holm, A. Thompson, V. Tikare, G. Wagner, E. Webb, X. Zhou, C. Garcia Cardona, A. Slepoy, Sandia report SAND2009-6226, October 2009.

45. F. Soisson, C.S. Becquart, N. Castin, C. Domain, L. Malerba and E. Vincent, J. Nucl. Mater. 406 (2010) 55–67
46. E. Vincent, C. S Becquart and C Domain, J. Nucl. Mater. 382 (2008) 154.
47. J. P. Hirth and J. Lothe, Theory of Dislocations (McGraw-Hill, New York, 1968).
48. Stroh, A.N., Philos. Mag. 3 (1958) 625–646.
49. P. Olsson, T. P. C. Klaver, and C. Domain, Phys. Rev. B. 81 (2010) 054102.
50. B. Yao, D. J. Edwards and R. J. Kurtz, J. Nucl. Mater. 434 (2013) 402.
51. Y. Wang, H. Y. Hou, X. B. Liu, R. S. Wang and J. T. Wang, http://arxiv.org/abs/1212.6900
52. Bacon, D. J., and Y. N. Osetsky, J. Nucl. Mater. 329-333 (2004) 1233.